NUMERICAL ANALYSIS OF THE MEASUREMENT OF NEAR BEAM ELECTRON CLOUD DENSITY AT KEKB LOW ENERGY RING

A Thesis
Submitted to the Faculty of the Graduate School
of Sokendai (The Graduate University for Advanced Studies),
in Partial Fulfillment of the Requirements for the degree of
Doctor of Philosophy

by
Puneet Jain
September 2010

The Graduate University for Advanced Studies (Sokendai)

The Graduate School

Puneet Jain

We, the dissertation committee for the above candidate for the Doctor of Philosophy degree, hereby recommend acceptance of the dissertation.

Dr. Hitoshi Fukuma (Supervisor)
Professor, Department of Accelerator Science
Sokendai

Dr. Kazuhito Ohmi (Chairperson)
Professor, Department of Accelerator Science
Sokendai

This dissertation is accepted by the Graduate School.

Director, KEK

ABSTRACT

Title of Document:	NUMERICAL ANALYSIS OF THE MEASUREMENT OF NEAR BEAM ELECTRON CLOUD DENSITY AT KEKB LOW ENERGY RING
	Puneet Jain, PhD, 2010
Supervised By:	Professor Hitoshi Fukuma, Department of Accelerator Science, Sokendai, Japan

A large number of electrons called an electron cloud are accumulated in beam chambers in positron storage rings. These electrons interact with the beam and can make it unstable. The density information of the electron cloud near the beam is therefore fundamental for studying the beam instabilities and mitigation techniques related to the electron cloud. Recently Kanazawa et al. proposed a method to measure the density of the electron cloud near the beam. The method measures high-energy electrons selectively by a retarding field analyzer located on a chamber wall, noting that the electrons near the beam get a strong kick by the beam. They calculated the density of the electron cloud simply assuming that the electrons that receive a kick are stationary.

We examined the measurement technique by a new computer code developed by us. The analysis showed that the volume near the beam occupied by the detected electrons, i.e. the observed volume, was strongly deformed due to the horizontal velocity of the electrons and nevertheless the observed volume calculated assuming the stationary electrons can still be used for calculating the density of the electron cloud in their measurement conditions. The modeling of electron cloud generation in

a field-free region of KEK B-Factory (KEKB) LER (Low Energy Ring), analysis of the measurement, comparison of the measured density with simulations and a possible improvement in the design of electron monitor are presented in details.

Table of Contents

List of Figures

Acknowledgements

First and foremost I offer my sincerest gratitude to my supervisor, Fukuma-sensei, who has supported me throughout my thesis with his patience and knowledge whilst allowing me the room to work in my own way. I will never forget his sincerity, hard work, availability for discussions even in late hours, and his invaluable guidance, which helped me to understand the subject. Throughout my three-year stay in KEK, he has been my inspiration to overcome all the obstacles in the completion of this research work, without him this thesis, too, would not have been completed in time.

I wish to thank Kurokawa-sensei, who not only selected me to pursue PhD from KEK but also provided me full financial support to participate in ECLOUD'07 workshop, held at S. Korea in April 2007, so that I get familiarize with the electron cloud subject before getting admitted in the graduate school. He had kind concern and consideration regarding my academic requirements even after his retirement.

I extend my sincere thanks to Ohmi-sensei for helping me in debugging my code innumerable times and also providing me computational support. In many ways I have learnt much from and because of him! I thank Kanazawa-sensei for having fruitful discussions with the results I used to get with my code.

I thank Professors G. Dugan (Cornell University, USA) and Miguel Furman (LBL, USA), who helped me understand electron cloud in great depth during my sabbatical to Cornell University, Ithaca, USA in October 2008.

I thoroughly enjoyed company of fellow Indian friends Abhay-san, Tyagi-san and Vijay-san. Tyagi-san kept us entertained with his huge repertoire of anecdotes and stories. A special thanks to Abhay-san for providing me help in getting colored graphs. In my daily work I have been blessed with a friendly and cheerful group of fellow students Demin-san and Semiya-san.

I thank KEK administrative staff members Aizawa-san, Miyai-san and Omura-san for being kind enough to help me in every possible way in non-academic matters due to my non-understanding of Japanese. I will always remember all of you throughout my life.

Last but not the least, I offer my regards to my parents for their blessings. A special thanks to my dear wife and daughter, whose love and moral support revitalized me in my tough times.

Chapter 1: INTRODUCTION

1.1 An overview of Colliders

In particle physics one gains knowledge about elementary particles by accelerating charged particle beams to very high kinetic energies and letting them impact on other particles. For sufficiently high energy, a reaction happens that transforms the particles into other subatomic particles. Detecting these products gives insight into the physics involved.

To do such experiments there are two possible setups:

- **Fixed target setup**: A beam of particles, i.e., the projectiles, is accelerated with a particle accelerator, and as collision partner, one puts a stationary target into the path of the beam.
- **Collider**: Two beams of particles are accelerated and the beams are directed against each other, so that the particles collide while flying in opposite directions.

The collider setup is harder to construct but has the great advantage that according to special relativity the energy of an inelastic collision between two particles approaching each other with a given velocity can be orders of magnitude higher if the collision velocity is near the speed of light. If the center-of-mass energy for the collision of two particles with energy E and rest-mass energy E_0 be represented by $E_{cm,collider}$ and $E_{cm,fixed}$ for a collider and fixed-target experiment respectively, then

$$E_{cm,collider}/E_{cm,fixed\ target} \approx \sqrt{2E/E_0}\ . \qquad (1.1)$$

It is clear that $E_{cm,collider} >> E_{cm,fixed}$ when $E >> E_0$, which is the case in high energy physics experiments. According to the types of particles, colliders are classified as

electron-positron colliders (circular or linear), proton-proton (anti-proton) colliders, electron-proton colliders, muon colliders and so on [1].

1.1.1 History of Colliders

The first proposal for a collider originated with a group at the Midwestern Universities Research Association [MURA]. This group proposed building two tangent radial-sector Fixed-Field Alternating Gradient accelerator (FFAG) rings [2]. Tihiro Ohkawa, one of the authors of reference [2], went on to develop a radial-sector FFAG accelerator design that could accelerate two counter rotating particle beams within a single ring of magnets [3]. The third FFAG prototype built by the MURA group was a 50 MeV electron machine built in 1961 to demonstrate the feasibility of this concept.

Gerard K. O'Neill proposed using a single accelerator to inject particles into a pair of tangent storage rings. As in the original MURA proposal, collisions would occur in the tangent section. The benefit of storage rings is that the storage ring can accumulate a high beam flux from an injection accelerator that achieves a much lower flux [4].

A (circular) collider usually consists of an injector, transport lines and a colliding storage ring. The injector provides the initial particles (e^+, e^-; p, p^+; e, p; μ^+, μ^-) for the storage ring. The beam lines transport the injected beam to the storage ring. The beams are injected into the ring by means of septa, kickers and separators. After the beams are filled, they are accelerated to the desired energy, squeezed, and brought into collision. As the beam loses intensity over its finite lifetime, after several hours, the ring needs to be refilled.

The first electron-positron colliders were built in Italy, at the Frascati laboratories near Rome, by the Austrian-Italian physicist Bruno Touschek. Around the same time, in the early 1960s, the VEP-1 collider was independently developed and built under supervision of Gersh Budker in the Soviet Institute of Nuclear Physics. Then shortly after, there was another built in Geneva, Switzerland. The colliders in the history of the world are listed in Table 1.

1.1.2 KEK B-factory: an electron-positron collider

In an electron-positron collider, high-energy collisions take place between e^+ and e^- beams. As seen in Table 1, most colliders ever built in the world are electron-positron colliders. The basic reason for this preference is that they provide "clean" collisions between two lepton beams. In particle physics, a B-factory is a collider-based storage ring designed to produce a large number ($\sim 10^9$) of B mesons and analyze their properties [5, 6].

The KEK B-factory (KEKB) is an asymmetric electron-positron collider for studying B-meson physics [7]. It consists of two rings, the low-energy ring (LER) for positrons with an energy of 3.5 GeV, the high-energy ring (HER) for electrons with an energy of 8 GeV, giving 10.58 GeV centre-of-mass energy, which is equal to the mass of Upsilon(4S).

Table 1 : Colliders in the world (DR: Double ring; SR: Single ring; LC: Linear collider)

Location	Name	$E_{cm,max}$ (GeV)	Start-up
Frascati, Italy	AdA ($e^+ e^-$ SR)	0.5	1962
	ADONE ($e^+ e^-$ SR)	3.0	1969
	DAΦNE ($e^+ e^-$ DR)	1.0	1997
Stanford/SLAC, USA	CBX ($e^+ e^-$ DR)	1.0	1963
	SPEAR ($e^+ e^-$ SR)	5.0	1972
	PEP ($e^+ e^-$ SR)	30	1980
	SLC ($e^+ e^-$ LC)	100	1989
	PEP-II ($e^+ e^-$ SR)	10.6	1999
Novosibirsk, Russia	VEP-1 ($e^+ e^-$ DR)	0.26	1963
	VEPP-2/2M ($e^+ e^-$ SR)	1.4	1974
	VEPP-4 ($e^+ e^-$ SR)	14	1979
Orsay, France	ACO ($e^+ e^-$ SR)	1.0	1966
	DCI ($e^\pm e^\pm$ SR)	3.6	1976
Cambridge, USA	CEA Bypass ($e^+ e^-$ SR)	6	1971
DESY, Germany	DORIS ($e^+ e^-$ DR)	6	1974
	PETRA ($e^+ e^-$ SR)	38	1978
	HERA ($e^\pm p$ DR)	160	1992
CERN, Europe	ISR (pp DR)	63	1971
	S p $\bar{p}$ S ($p\,\bar{p}$ SR)	630	1981
	LEP ($e^+ e^-$ SR)	190	1989
	LHC (pp DR)	14000	2004
Brookhaven, USA	RHIC (heavy ions DR)	200/u	1999
	RHIC (pp DR)	500	
Cornell, USA	CESR ($e^+ e^-$ SR)	12	1979
KEK, Japan	TRISTAN ($e^+ e^-$ SR)	60	1986
	KEKB ($e^+ e^-$ DR)	10.6	1999
Beijing, China	BEPC ($e^+ e^-$ SR)	5.6	1989
Fermilab, USA	Tevatron (pp DR)	1000	1987

1.2 General scheme of KEKB

The construction of KEKB started in 1994, utilizing the existing tunnel for TRISTAN, a 30 GeV × 30 GeV electron–positron collider. After 32 months of dismantling of TRISTAN, the construction of KEKB was completed in November 1998, and commissioning started in December 1998 [8 - 10]. Two 3016 m long rings, an 8-GeV electron ring (HER) and a 3.5-GeV positron ring (LER) are installed side by side in a tunnel 11 m below the ground level. Their injector, which is a linac-complex, provides the rings with not only an electron beam, but also a positron beam. The two rings cross at one point in the "Tsukuba area", called the interaction point (IP), where electrons and positrons collide. The Belle detector surrounds the IP to catch particles produced by the collisions. Just opposite to the IP the two rings pass each other at different heights, and the electrons and positrons do not collide. Fig. 1.1 shows a schematic layout of KEKB.

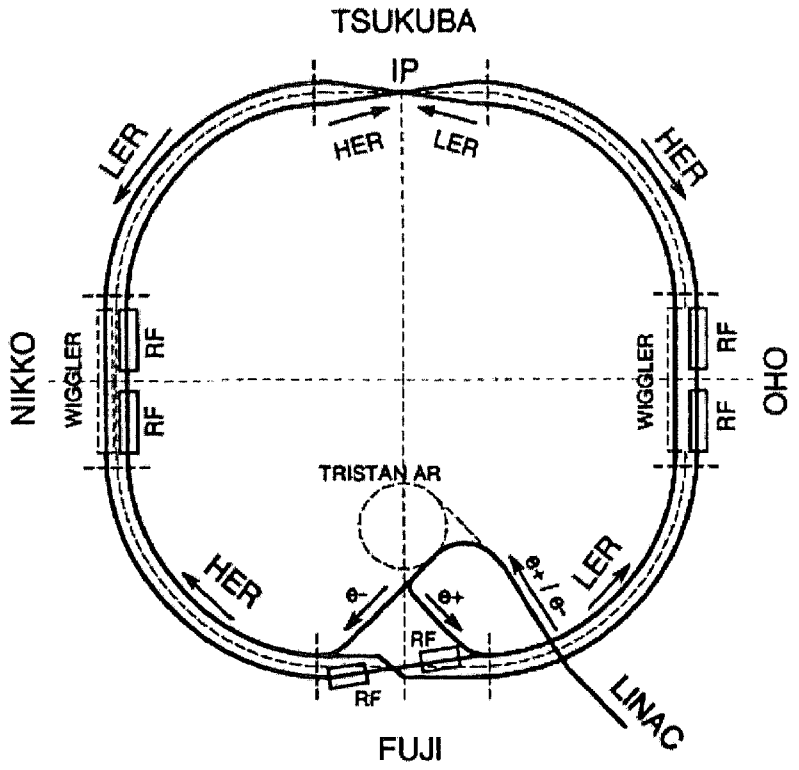

Fig. 1.1. Schematic of layout of KEKB.

1.2.1 Luminosity boost

In order to obtain high luminosity, the stored currents in the rings should be as high as possible, and the beam sizes at the IP should be as small as possible. In KEKB, the design currents in the rings are 1.1 A in the HER and 2.6 A in the LER. The beam is distributed among about 1584 bunches with a bunch spacing of 1.84 m. The beta-function at the IP is 120 cm in the horizontal direction and 0.59 cm in the vertical direction. The estimated vertical beam size at IP is 0.94 μm. In the 2009 run through June 17, KEKB marked the following records of the luminosity: peak luminosity, 21.08 nb^{-1} s^{-1}; integrated luminosity/day, 1.479 fb^{-1}; integrated luminosity/7 days, 8.428 fb^{-1}; integrated luminosity/30 days, 30.208 fb^{-1}. The numbers above are all recorded values by the Belle detector.

1.2.2 Storage of high currents, vacuum chambers and cavities

These high currents stored in the rings may excite strong coupled-bunch instabilities. The main issue is, therefore, how to store such large currents in the rings and at the same time to maintain stable collisions between the electron and positron beams. Both the KEKB rings have copper vacuum chambers that can sustain a high heat load of synchrotron radiation. The HER vacuum chambers have a race-track shape, whereas those of LER have a round shape with an inner diameter of 94 mm. This large diameter is effective to lower the growth rate of coupled bunch instabilities due to the resistive-wall impedance.

The beam excites the fundamental mode and higher-order modes (HOM) in a cavity. The fundamental mode is the lowest-frequency mode, and is used for acceleration, whereas HOMs are modes with higher frequencies. In a small ring, only HOMs are

responsible for coupled-bunch excitation; however, in a large ring with a high stored current, the fundamental mode also becomes responsible for instability. KEKB uses two kinds of HOM-free cavities: normal conducting cavities, called ARES, for the LER and HER, and superconducting cavities (SCC) for the HER.

ARES is an acronym of accelerator resonantly coupled with energy storage. It consists of three cells: an accelerating cell, an energy-storage cell, and a coupling cell between them. HOMs are extracted from the cavity by four wave guides attached to the accelerating cell, and are absorbed by SiC absorbers equipped at the end of the wave guides. Beam pipes attached to the cell are grooved to make those HOMs, which cannot be extracted by the waveguides, propagate towards the beam pipes. The large-volume, low-loss energy-storage cell effectively increases the stored energy of the cavity system.

The superconducting cavity for KEKB has two large-bore beam pipes that are attached to both ends of the cavity cell. The diameters of the beam pipes are chosen so that the frequencies of all modes, except for the fundamental one, become higher than the cut-off frequencies of the pipes. HOMs propagate towards beam pipes and are eventually absorbed by ferrite dampers attached to the inner surfaces of the pipes.

1.2.3 Finite-angle crossing at IP

One of the salient features of KEKB is the adoption of a finite-angle crossing at the IP, where the electron and positron bunches collide at a finite angle of ±11 mrad. This scheme does not require any separation dipole magnets and makes the interaction region much simpler than in head-on collision scheme. Another advantage is that bunches are separated quickly after the collision, allowing a minimal bunch

spacing of 59 cm. KEKB's leading finite crossing angle interaction design provides its high luminosity.

Currently, the KEKB is shut down for its upgrade to SuperKEKB. The physics from SuperKEKB will be complementary to that which can be obtained from LHC. The upgrade of KEKB using the low emittance option will study CP asymmetry and new sources of flavor mixing in the quark sector [11].

1.3 Beam instability in the LER

During its early commissioning, the luminosity of KEKB was limited by the vertical beam blow-up [12, 13]. The beam as a function of beam current started to increase at a threshold beam current and was almost doubled at 300 mA under typical operating conditions. This blow-up is one of the most serious problems limiting the luminosity of KEKB. The main characteristics of the observed beam blow-up were:

i) single beam and a multi-bunch effect,
ii) no dipole oscillation was observed when the vertical chromaticity was high [14],
iii) the blowup had a threshold which was determined by the charge density (bunch current/bunch spacing),
iv) the blowup was almost independent of betatron tunes, and
v) no blowup was observed in the horizontal plane.

A model to explain the blowup was proposed by F. Zimmermann and K. Ohmi [15]. In their model, the blowup was explained as a single-bunch head–tail instability due to a large number of electrons produced by photoemissions or secondary emissions. The collection of these electrons is called an electron cloud. Strong or regular head-tail instability in a bunch occurs by the mediation of the cloud. The observed beam size blow-up resulted due to head-tail oscillation of the instability. The tune shift was

roughly consistent with a calculation based on the model, and the threshold bunch-intensity of the blowup was consistent with the threshold of the transverse mode-coupling instability [16].

1.4 Electron Cloud

A collection of electrons can be formed in positron and proton storage rings. Seeds of these electrons are slow electrons produced by synchrotron radiation (SR), ionization of the residual gas (a small effect in the e^+-e^- factories) or by secondary emission. In the secondary emission process the low-energy background primary electrons, typically 10s of electron volts, already present in the chamber are driven by the electric field of the beam into the chamber with sufficient kinetic energy to generate secondary electrons on the wall. Hence, this is a type of multipacting process.

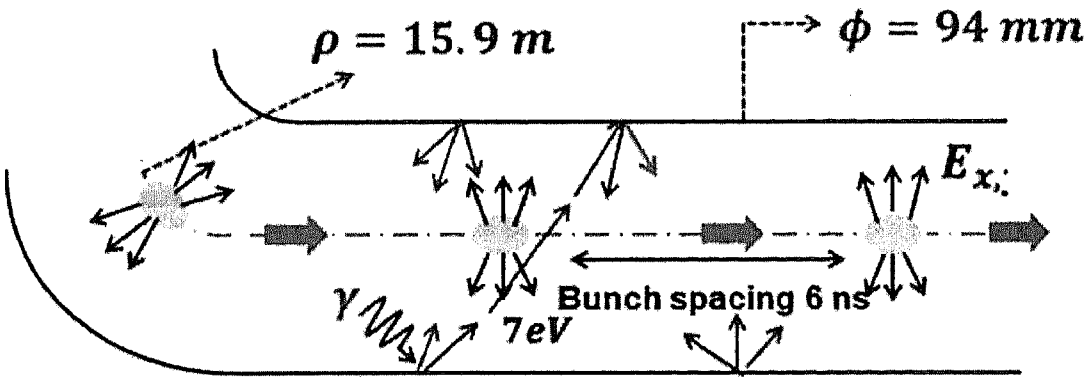

Fig. 1.2. Schematic of electron multiplication.

A schematic of electron multiplication in KEKB LER is shown in Fig. 1.2. The electrons get a kick from the electric field of the positron bunch, the strength of which

depends on the position of the electron from the bunch. These electrons, with an increased kinetic energy, hit the opposite end of the wall, produce secondary electrons there before getting lost.

If the number density of the electrons becomes sufficiently large, they can lead to degradation of the particle beam either by direct interaction or through electron-stimulated desorption of gases. The dense pockets of electrons are termed as an electron cloud (EC), and the resulting corruption of the beam is termed as electron cloud instability (ECI) [17]. The charge distribution of the electron cloud responds to the position of a passing bunch. In turn, the electric field of the electron cloud perturbs subsequent bunches, creating a bunch-to-bunch coupling which can drive transverse multi-bunch instabilities. The multi-bunch instability is broadband, involving many modes. The EC can also couple the head of a bunch to its tail, creating a single-bunch head-tail instability (which, however, requires the presence of many bunches in the machine to generate the EC) [15]. Apart from causing bunch instability, the EC can have damaging effects on the accelerator performance such as the increased thermal load to chamber walls of superconducting accelerators, emittance blow-up, gas desorption from chamber walls and so on [18, 19]. The EC couples most strongly to a positively charged beam, because the space charge of a negative beam repels the EC. Since the EC effect is one of the big concerns in existing accelerators and a potential threat to future accelerators such as Super B-factories and a damping ring of the linear collider, much effort has been made to study the effects and find mitigation methods against it.

1.4.1 Experimental observations of EC

Early observations of instabilities correlated with pressure are attributed to EC in proton rings and coasting beams. Perhaps the first ever observation of an EC driven instability was made with a bunched beam at a small proton storage ring of the BINP, Novosibirsk around 1965 [20]. The ring circumference was only 2.5 m. Coherent betatron oscillations and beam losses occurred above a threshold proton intensity of 1 to 1.5×10^{10}. Budker and co-workers identified the instability as one due to electrons. At about the same time as in Novosibirsk, a vertical instability, which is now attributed to electron cloud, was observed at the Argonne ZGS [21]. The instability growth time varied between 5 and 100 ms, and the intensity threshold from 2 to 8×10^{11} protons distributed over eight equally spaced bunches. In 1965, an electron-related instability affected operation of the BNL AGS [22]. A coherent vertical betatron oscillation led to beam loss. At about the same time, pressure-dependent instabilities were observed at Orsay, which were attributed to nonlinear fields introduced by particles with a charge sign opposite to that of the beam (i.e., electrons or ions, depending on the beam charge) [22]. In 1971, the Bevatron also suffered from an electron-driven instability, in this case for a coasting beam [23]. The observation of electron-cloud instabilities in coasting beams at the CERN ISR was made in 1972. The instability had a fast rise time and lasted for 5 to 10 ms [24]. Similar observations of ECI in LANL proton storage ring (PSR) were made in 1988 [25, 26]. An important characteristic of the PSR instability was the occurrence of sustained coherent oscillations below the loss threshold and the observation of an intense electron flux on the beam pipe wall at the end of a bunch passage. The progression of the instability from the end of the bunch towards the front suggested that for the PSR electron production and instability should be considered as a combined process.

It was in 1989 that the KEK Photon Factory (PF) switched from electron to positron operation. The positron beam suffered from a wideband vertical multi-bunch instability which had not been seen with electron beams [27]. The unstable mode pattern of this instability was characteristic of a wakefield extending only over a few bunches. The instability, which was first time observed in positron rings, was interpreted as one driven by photoelectrons [27]. In an attempt to model this phenomenon quantitatively, detailed computer simulations of the electron build-up inside a vacuum chamber and the resulting wakefield were performed [28]. This investigation at the KEK PF was probably the first one which revealed an EC effect for lepton beams, and it ushered in the ''modern era'' of the effect, sparking substantial and widespread interest.

Anomalous transverse coupled bunch instability had been observed in mid 1980s in Cornell Electron Storage Ring (CESR) [29]. The growth rate of the positron beam was very reproducible and was independent of the residual gas pressure. The instability was however not as reproducible for electrons. The anomalous instability was present only when the distributed ion pumps (DIPs) were powered [30]. It disappeared immediately when the DIPs are turned off. The growth rate was proportional to the number of DIPs powered and to the DIP anode voltage [31]. The observations were consistent with the hypothesis [32 - 34] that slow electrons trapped in the beam chamber were responsible for the anomalous instability. These electrons were produced primarily through photoemission and were trapped in the combined dipole magnetic field and quadrupole electrostatic leakage field from the DIPs. This "trapped photoelectron instability" had a very long range, was nonlinear in beam current, and was predominantly horizontal.

In contrast with the trapped photoelectron instability observed in CESR, the instability observed in the PF of KEK was "free photoelectron instability" (electron cloud instability or "ECI"). This instability, in contrast with the CESR instability,

occurred in the absence of magnetic and electrostatic fields; was strong in the vertical direction; and increased with beam current. It was short-range in nature, because the photoelectrons moved rapidly to the chamber walls.

In 1996, a series of EC experiments were conducted by an IHEP-KEK collaboration at the Beijing Electron Positron Collider (BEPC) [35]. Later, the photoelectron instability was reported in BEPC and KEKB [36, 37]. Shortly thereafter, crash programs were launched for the positron ring of the PEP-II B Factory [38] and, after simulations and analytical estimates had predicted a serious effect for heat load and beam stability [18, 19], for Large Hadron Collider (LHC) [39]. The possibility of beam-induced multipacting in the LHC was first mentioned by Gröbner in 1996 [40]. Since 1998, EC effects have been seen with the LHC test beam in the super-proton ring (SPS) as well.

1.4.2 Mitigation techniques to control EC

Secondary electrons, which are generated in a multiplication process, play a large part in the formation of EC. Various experiments, therefore, have been performed to suppress the multiplication of secondary electrons [41-44] as well as the generation of photoelectrons [45-48]. There are two approaches for suppressing the EC effect: the first is to modify the chamber surface properties such that the secondary electron yield (SEY) is reduced, if possible below unity. This can be atleast partially achieved by conditioning the vacuum chamber surface by exposing it to a deliberately generated EC over an extended period, which is often called beam scrubbing [49]. An effective approach to suppress the multiplication of secondary electrons is to utilize a beam duct with an inner surface with a low SEY. Many kinds of surfaces, like nonevaporable getter (NEG) materials and TiN, have been studied so

far [50, 51]. The second approach consists in changing the dynamics of the EC by externally applied electric, magnetic, or electromagnetic fields. Solenoids have been shown to confine the electrons close to the chamber wall and eliminate the EC in straight sections of several machines [52-54], but they cannot be applied in bending sections.

Clearing electrodes allow a static electric field to be applied, which changes the trajectories of the electrons and may disturb the EC buildup. Electromagnetic fields were also proposed for electron cloud clearing. Clearing electrodes have been successfully used in several machines for electron or ion clearing [55, 56].

A drastic reduction of the SEY has been reported with a metallic grooved surface having a specially designed grooved profile [57-59]. Such a surface reduces the escape probability of secondary emitted electrons, reducing considerably the effective SEY. Grooved surfaces are effective to suppress the secondary electron emission, and can be a promising technique to mitigate the electron cloud effect in positron/proton storage rings. It has been recently demonstrated for the first time that there is a large reduction in the measured electron density with the installation of the clearing electrode and the groove structures [60].

Antigrazing surfaces have been designed for LHC to reduce the photoemission rate from grazing incident photons. They have also been tested in RHIC to reduce the beam-stimulated molecular desorption [61, 62]. The data showed that the vacuum pressure rise was reduced by over an order of magnitude at the location of the collimator. In addition to passive measures, active feedback is also a possible cure for EC-induced instabilities. The instability threshold was observed to increase by 20-25% with the prototype feedback system [63].

1.4.3 Electron cloud density measurements

The knowledge of electron cloud density (ECD) is essential to the study of the EC effects. Several quantitative measurements of ECD have been reported. A pulsed electrode called an electron sweeper was used to sweep electrons towards a detector at PSR [64]. An absolute measurement of ECD has been carried out at HCX by measuring ions expelled by the beam whose kinetic energy at the wall is related to a beam potential decreased by the EC [65]. A phase shift of the TE wave caused by the EC was used to measure ECD at PEP-II [66]. These methods give an average ECD in the beam chamber. However, the measurement of the ECD near the beam is more important than the average ECD for the study of the single-bunch instability caused by the EC because the beam interacts with the EC near the beam, thus inducing the instability.

Recently, Kanazawa et al. have proposed a method of measuring the ECD near the beam and reported a result of the measurement in LER at KEKB [10, 67]. It is based on an idea to measure EC current above a threshold energy using a retarding field analyser (RFA) located on the chamber wall. The high-energy component of the electrons is expected to have originated from a region near the beam because a strong kick by the beam is given to the electrons close to the beam. A unique point of the method is that it measures the density of the electrons with which the beam really encounters. No laboratory other than KEK has reported EC density measurement seen by the beam. Although the method gives a possibility to measure the ECD near the beam, Kanazawa et al. [67] estimated near-beam ECD under simple assumptions that the electrons are stationary and that they hit the wall as a result of the single kick received from the beam. However, in reality, the electrons have finite velocity and some electrons detected by the monitor will originate from non-central parts of the chamber.

In this thesis, we examine the above assumptions in detail using a newly developed simulation code. Though a number of codes are available for EC study, the first and the pioneering code PEI (K. Ohmi) followed by others viz. POSINST, ECLOUD, WARP, HEADTAIL, PEHT etc., the need of doing special tasks inspired us to write our own code, which is dedicated to near-beam ECD studies only. The newly developed code has special functions such as a backtrack routine for tracking the trajectory of a detected electron to a position immediately before the kick by the beam and a routine for the calculation of ECD seen by the beam.

In all results presented here, we assume that there is no offset in the beam position from its design trajectory. Only photoelectrons have been considered as the source of seed electrons because the photoelectrons are main source of primary electrons in positron storage rings. We carried out the analysis only in drift space.

We organize the thesis as follows. Chapter one is the introduction. The simulation model of the EC build-up is described in chapter two. The experimental procedure to measure near-beam ECD and the analysis of the measurement technique along with its validity is mentioned in chapter three. The conclusion is given in chapter four.

Chapter 2: BUILDUP OF ELECTRON CLOUD

An overview of the physics involved in the build-up of electron cloud (EC) and its modeling in simulations is presented in this chapter.

2.1 Generation of primary electrons

Primary electrons are generated on the inner surface of the LER chamber during a bunch passage by three processes: photoemission, ionization of the residual gas and generation of electrons due to beam loss in the chamber walls. In e^--e^+ colliders, the source of primary electrons is mainly the photoelectrons. We therefore modeled only the photoelectrons as the source of primary electrons in our simulation code.

2.1.1 Number of photoelectrons per positron bunch

A positron bunch, when passing through a dipole bending magnet (BM), emits synchrotron radiation (SR) that strikes the chamber wall and generates photoelectrons. The basic quantity to compute is the number of photoelectrons per bunch per radian of the bending angle generated on the inner surface of the chamber wall from the SR light photons hitting it directly and by multiple reflections from the surrounding wall.

$$\frac{dN_{p.e./bunch}}{d\theta} \approx \eta_e N_{e^+} \frac{dN_{\gamma/e^+}}{d\theta} \approx \eta_e N_{e^+} \frac{5\alpha\gamma}{2\sqrt{3}}. \qquad (2.1)$$

Such a quantity, expressed in eq. (2.1), is a product of photoelectron yield η_e and the photoemission rate $N_{e+}\, dN_{\gamma/e+}/d\theta$ [68]. Here α is the fine structure constant; γ is the relativistic factor of positron, and N_b is the positron bunch population. The photoelectron yield η_e depends on the photon energy E_{crit}, where,

$$E_{crit} = 3\gamma^3 \hbar c/2\rho, \qquad (2.2)$$

where ρ is the radius of curvature of BM. For KEKB LER, ρ =15.9 m, γ =6850.44, therefore $E_{crit} \approx$5.97 keV.

For many materials, the η_e can be approximated as a constant, of the order of 0.1, over a fairly large energy range of photons, e.g., between a few eV and a few 10s of keV [69]. The energy and direction of the emitted photon from the positron bunch can be calculated from the standard SR formula [70]. Knowing the energy of the incident photon and its angle of incidence relative to the local normal to the vacuum chamber, the scattering probability of the incident photon can be computed. The sources of photoelectrons at any transverse plane down a BM are the main SR light emanating from the bunch and scattered SR light.

The electron monitor is mounted on a vacuum pump port of the LER chamber to measure the EC current. The electrons enter into it through two 10-cm-long longitudinal openings, i.e., the RFA entrance on the LER chamber. Due to the ultra relativistic speed of the bunch, the photons are emitted in a vertical strip, tangent to a bunch, from a BM and strike the LER chamber longitudinally with varying intensity depending on its angular position inside the BM. The SR fan, which strike a 10-cm-long RFA entrance, shown in red colored line in Fig. 2.1, subtend an angle of $\Delta\theta \sim$ 8.93 μrad at a distance of 23 m down the BM in a field-free region (drift space) at the bunch position inside the BM.

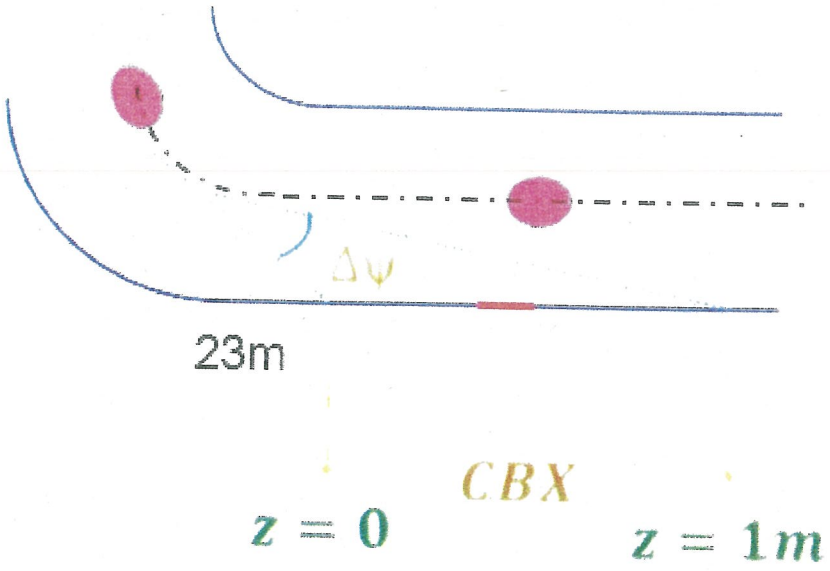

Fig. 2.1. Schematic drawing of generation of photoelectrons in a drift space by a single positron bunch.

The average number of photoelectrons, generated on the chamber wall at the location of RFA entrance, per positron bunch passage from the BM (Fig. 2.1) is given by [68]

$$N_{p.e./bunch} = \frac{dN_{p.e./bunch}}{d\theta}\Delta\theta = \eta_e N_{e^+} \frac{5\alpha\gamma}{2\sqrt{3}}\Delta\theta. \qquad (2.3)$$

The bunch population $N_{e+} = i_B / q / f_{rev}$, where i_B is the bunch-current and q is the electronic charge. The revolution frequency, f_{rev}, of positron bunches is 99.4 kHz; therefore, for example, for 1 mA bunch current there are 6.3×10^{10} positrons in a bunch. The bunch generates more than four million photoelectrons on the LER chamber wall corresponding to a horizontal opening angle of $\Delta\theta \sim 8.93$ μrad at the RFA entrance using eq. (2.3).

Since the entire beam-pipe is filled with the EC of varying intensity along z-axis, i.e., the beam propagation direction, we considered a longitudinal numerical box of one-meter length placed around the RFA entrance for better statistics of macro-electrons

in the EC build-up. We shall refer this box as 'Computational-Box' (CBX). The bunch generates > 10^8 photoelectrons on the LER chamber wall inside the CBX, corresponding to a horizontal opening angle represented by $\Delta\psi$ in Fig. 2.1. Since this number is fairly large to handle even by a super computer, we simulated a smaller number of representative electrons referred to as the macro-electrons. The charge-to-mass ratio of a macro-electron is same as that of a real electron. In simulations, we represented this fact by a parameter '*ftf*' defined as

$$ftf = \frac{Number\ of\ actual\ electrons}{Number\ of\ macro-electrons}\ ;typically\ 1000$$

2.1.2 Position assignment of the photoelectrons

A positron bunch, while passing through a dipole BM emits SR light that strikes the entire chamber wall length. The photoelectrons are produced at the inner surface of the LER chamber wall with η_e set as 0.1 in our simulation model for copper surface. The launch positions of the macro-photoelectrons on the inner surface of the chamber wall were chosen to be a Gaussian distribution in a median plane within an open angle of $\pm 1/\gamma$ (rad) centered at the bunch. The actual open angle is different from a Gaussian, but for simplicity of the model, we preferred it because it is not sensitive to our analysis [70].

In our simulation model we assumed that there is no transverse displacement of the bunch from the design orbit.

Following the coordinate system as shown in Fig. 2.2, the y-coordinate of a macro-photoelectron was assigned as $y = y_{max} \times$ random number weighted with a Gaussian of 1-σ, and, the x-coordinate as $x = -\sqrt{(r_{chm}^2 - y^2)}$, where y_{max} is the maximum absolute

value of the y-coordinate of the photoelectrons generated by the main SR light hitting the chamber wall and r_{chm} is the radius of the chamber wall. The transverse positions of the macro-photoelectrons at a given z are shown with pink dots in Fig. 2.2 having a Gaussian profile centered on x=0. A uniform longitudinal distribution of macro-photoelectrons was assumed in the CBX, so that the z-coordinate of a macro-photoelectron was given by a random number uniformly distributed over the CBX length.

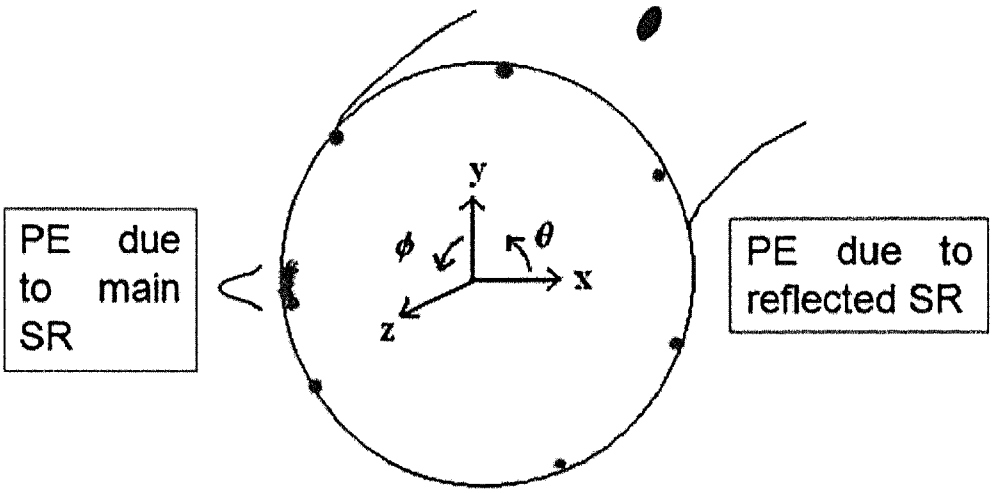

Fig. 2.2. Reference co-ordinate system.

2.1.3 Velocity assignment of the photoelectrons

The photons from the SR light lose their energy to the chamber wall upon hitting it and are lost. They knock out photoelectrons on the inner surface of the chamber wall. The velocities of the newly generated photoelectrons do not have any correlation with the direction of the incident photons. The macro-photoelectrons were assumed to emit with a cosine distribution [71, 72], the angle being measured from the normal to the surface, i.e.

$$\frac{dN}{d\Omega} \propto cos\theta \rightarrow \frac{dN}{d\theta\, d\phi} \propto cos\theta\, sin\theta, \qquad (2.4)$$

where θ ($0 < \theta < \pi/2$), the angle of inclination, is with respect to the x-axis and ϕ ($0 \leq \phi \leq 2\pi$), the azimuth angle, is with respect to the z-axis as defined in Fig. 2.2. Using Monte-Carlo sampling technique the 'θ's and 'ϕ's were generated to give aforesaid angular distribution of the photoelectrons.

The initial energy distribution of the macro-photoelectrons was chosen as a Gaussian with a peak at 7 eV and an rms spread of 5 eV [73]. In simulations it was done by using a random number generator weighted with a Gaussian (multiplied by 7) of 5-σ standard deviation. Thus knowing the absolute velocity value v along with its direction, the velocity components of the macro-photoelectrons are given by

$$v_x = v\cos\theta,$$

$$v_y = v\sin\theta,$$

$$v_z = v\sin\theta\sin\phi. \qquad (2.5)$$

The cross-section of the beam-pipe is circular. All the macro-photoelectrons with nonzero y-coordinates have transverse velocities with respect to the circular boundary of the beam-pipe. These velocities were modified by a rotation-transformation so as to get them with respect to the origin at the centre of beam-pipe. Fig. 2.3 shows a schematic drawing of the velocity component transformation. If the velocity components of an electron generated at any arbitrary location, say O_1 (x, y), given by eq. (2.5), are represented by (v_{x1}, v_{y1}), then the velocity components with respect to the origin O, the centre of the LER chamber, represented by (v_x, v_y) are given by

$$\begin{bmatrix} v_x \\ v_y \end{bmatrix} = \begin{bmatrix} \cos\alpha & \sin\alpha \\ -\sin\alpha & \cos\alpha \end{bmatrix} \begin{bmatrix} v_{x1} \\ v_{y1} \end{bmatrix}, \qquad (2.6)$$

where $\alpha = \sin^{-1}(y/r_{chm})$. There is no change in v_z, as the coordinate transformation is a rotation about the z-axis.

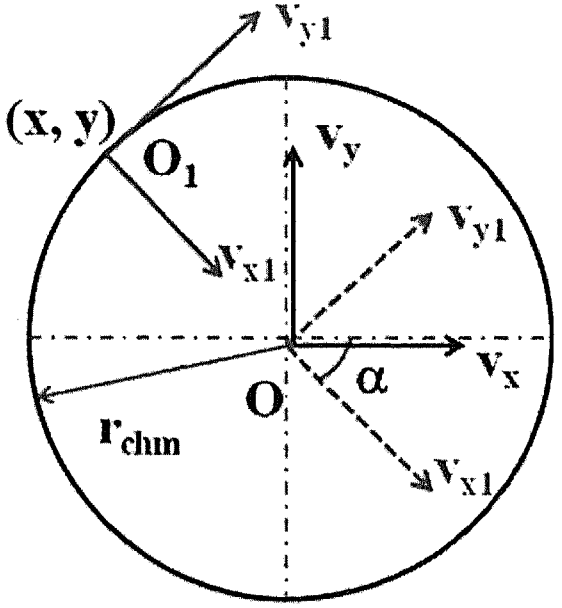

Fig. 2.3. Schematic of velocity transformation about z-axis with respect to an origin $O_1(x, y)$.

2.1.4 Photoelectron generation from the reflected SR light

We mentioned in sec. 2.1.1 that the inner surface of the LER chamber also gets illuminated by the scattered SR light. The exact modeling of the scattered photons from a nonplanar surface is quite complex [74, 75]. The generation of the photoelectrons from the absorbed photons around the chamber wall depends on the surface smoothness of the chamber wall for the reflection of the SR light. For a slow build up of the EC, the sources of the photoelectrons should be a minimum. Thus, inside the bending magnets a low photon reflectivity is desirable, since the magnetic field confines the photoelectrons emitted at the outer side of the chamber, which is the primary impact point of SR, to the vicinity of the wall.

The launch positions of the macro-photoelectrons from the reflected SR light were assumed to be a uniform distribution along the periphery of the inner chamber wall. The reason for the uniform distribution consideration was the large distance of the location of the RFA entrance from the BM, 23 meters in our case, and at large distances the chamber wall gets illuminated by the scattered photons approximately uniformly. The transverse positions of the macro-photoelectrons by the reflected SR light are shown with circular dots on the periphery of the chamber at a given z in Fig. 2.2. We chose a reflectivity of 0.2 in our simulation model [48]. The velocity assignment was done similar to the photoelectrons generated from the main SR light.

2.2 Beam-electron interaction

An electron of the EC interacts with positron bunches, receives a transverse kick via Coulomb force and gains kinetic energy. We present a framework for the kick exerted by a positively charged Gaussian bunch to an electron in accordance with Bassetti-Erskine [76] formalism for the purpose of our simulations.

Consider an ultra relativistic Gaussian positron bunch (β = v/c $\approx$ 1) moving in the longitudinal direction. We define this direction by z-axis (Fig. 2.2). The charge density within the bunch can be expressed as

$$\rho(x,y,z) = \frac{Q}{(2\pi)^{3/2}} \frac{1}{\sigma_x \sigma_y \sigma_z} e^{\left(-\frac{x^2}{2\sigma_x^2}\right)} e^{\left(-\frac{y^2}{2\sigma_y^2}\right)} e^{\left(-\frac{z^2}{2\sigma_z^2}\right)}, \tag{2.7}$$

and the total charge Q by

$$Q = N_b e = \iiint \rho(x,y,z)\, dx\, dy\, dz, \tag{2.8}$$

where e is the electronic charge and N_b is the bunch population. To evaluate the electrostatic potential, represented by $\phi(x, y, z)$, and created by the bunch-charge distribution, following the Poisson's equation, the potential can be expressed as

$$\nabla^2\phi(x,y,z) = -\rho(x,y,z)/\varepsilon_0. \tag{2.9}$$

The solution is

$$\varphi(\vec{x}) = \frac{1}{4\pi\varepsilon_0}\int d\vec{x'}\,\frac{\rho(\vec{x'})}{\left|\vec{x}-\vec{x'}\right|}. \tag{2.10}$$

2.2.1 Equations of motion for test electron of EC

Consider an integral

$$I = \int_0^\infty du\, e^{\left(-u^2\left|\vec{x}-\vec{x'}\right|^2\right)}. \tag{2.11}$$

Analytically, the solution of the integral of eq. (2.11) is given as

$$I = \frac{\sqrt{\pi}}{2\left|\vec{x}-\vec{x'}\right|}. \tag{2.12}$$

Therefore

$$\left|\vec{x}-\vec{x'}\right| = \frac{2}{\sqrt{\pi}}\int_0^\infty du\, e^{(-u^2\,|\vec{x}-\vec{x'}|^2)}. \tag{2.13}$$

Substituting $u^2 \rightarrow 1/q$; ('q' being a new variable) in eq. (2.10), the potential can be rewritten as

$$\varphi(\vec{x}) = N_b \frac{e}{4\pi^{3/2}\varepsilon_0} \int_0^\infty dq \frac{e^{-\frac{x^2}{q+2\sigma_x^2}}}{(q+2\sigma_x^2)^{1/2}} \frac{e^{-\frac{y^2}{q+2\sigma_y^2}}}{(q+2\sigma_y^2)^{1/2}} \frac{e^{-\frac{z^2}{q+2\sigma_z^2}}}{(q+2\sigma_z^2)^{1/2}}. \qquad (2.14)$$

It follows from classical electrodynamics [77], that the electric field for an ultra-relativistic charged particle is Lorentz contracted.

In bunch-frame of reference, all the charged particles are static; hence only an electrostatic field is associated with it. Since a test electron from the EC witnesses the electromagnetic (EM) field carried by the moving bunch in lab-frame, it is therefore necessary to evaluate the fields associated with the bunch in lab-frame. The EM fields in bunch frame are denoted by (E_{x1}, E_{y1}, E_{z1}), (B_{x1}, B_{y1}, B_{z1}) and that in the lab-frame by (E_x, E_y, E_z), and, (B_x, B_y, B_z).

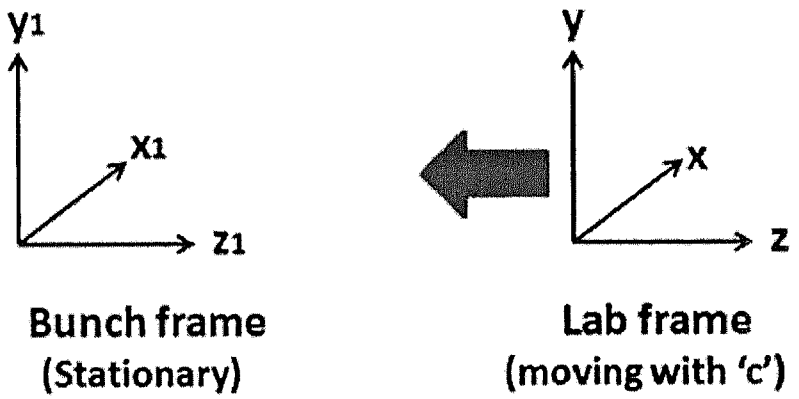

Fig. 2.4. A schematic of Lorentz transformation.

The bunch moves at an energy of 3.5 GeV whereas the electrons from the EC have kinetic energies of ~ 2 keV. Therefore, the electrons can be treated as stationary compared to the bunch. In order to find the EM fields carried by an ultra-relativistic bunch, we treat the lab-frame to be moving with a speed of -c along z-direction with respect to the stationary bunch-frame (Fig. 2.4). The EM fields in the two inertial frames are related by

$$E_z = E_{z1}\,, \qquad E_x = \gamma\left(E_{x1} + c\,B_{y1}\right), \qquad E_y = \gamma\left(E_{y1} - c\,B_{x1}\right),$$

$$B_z = B_{z1}\,, \qquad B_x = \gamma\left(B_{x1} - c^{-1}\,E_{y1}\right), \qquad B_y = \gamma\left(B_{y1} + c^{-1}\,E_{x1}\right). \qquad (2.15)$$

In bunch-frame there is no magnetic-field associated with the bunch; B_{x1}, B_{y1} and B_{z1} are all = 0. Therefore, in lab-frame, the electromagnetic field, associated with the ultra-relativistic bunch, is given by [from eq. (2.15)]

$$E_x = \gamma E_{x1}\,, \qquad E_y = \gamma E_{y1}\,, \qquad E_z = \gamma E_{z1}\,,$$

$$B_x = -\gamma\,E_{y1}/c\,, \qquad B_y = \gamma\,E_{x1}/c\,, \qquad B_z = B_{z1} = 0. \qquad (2.16)$$

The Lorentz-transformation of the position coordinates is $x_1 = x$, $y_1 = y$ and $z_1 = \gamma(z - c\tau)$, where 'τ' is the proper-time, $\{x_1, y_1, z_1\}$ are bunch-frame position coordinates and $\{x, y, z\}$ are lab-frame coordinates.

The electric-field components in bunch-frame are given by

$$E_{x1} = -\frac{\partial\varphi(x1, y1, z1)}{\partial x1}, E_{y1} = -\frac{\partial\varphi(x1, y1, z1)}{\partial y1}, E_{z1} = -\frac{\partial\varphi(x1, y1, z1)}{\partial z1}. \qquad (2.17)$$

The x-component of the electric-field in lab-frame is given by [using eqs. (2.14), (2.16) and 2.17]

$$E_x = \frac{N_b\, e}{2\,\pi^{\frac{3}{2}}\,\varepsilon_0}\,\gamma\, x \int_{q=0}^{\infty} dq \frac{e^{-\frac{x^2}{q+2\,\sigma_x^2}}\; e^{-\frac{y^2}{q+2\,\sigma_y^2}}\; e^{-\frac{\{\gamma\,(z-c\tau)\}^2}{q+2\,\gamma^2\,\sigma_z^2}}}{(q+2\sigma_x^2)^{\frac{3}{2}}\,(q+2\sigma_y^2)^{\frac{1}{2}}\,(q+2\,\gamma^2\sigma_z^2)^{\frac{1}{2}}}. \qquad (2.18)$$

The x-equation of motion of a test electron of the EC is given by

$$\frac{dp_x}{d\tau} = -\,e\left[E_x + \left(v_y B_z - v_z B_y\right)\right] = -eE_x\,\left(1-\frac{v_z}{c}\right), \qquad (2.19)$$

where v_y and v_z are the velocity components (all non-relativistic) of the test electron. Under the 'impulse-approximation', the momentum change is obtained by integrating the force equation over time assuming that the test electron does not move during the bunch passage; i.e.

$$\Delta p_x = \int_{-\infty}^{\infty} d\tau\, \frac{dp_x}{d\tau} = -\,\frac{N_b e^2 \gamma x}{2\pi^{3/2}\varepsilon_0}\,\frac{\sqrt{\pi}}{\gamma c}\left(1-\frac{v_z}{c}\right)\int_0^{\infty} dq \frac{e^{-\frac{x^2}{q+2\sigma_x^2}}}{(q+2\sigma_x^2)^{3/2}}\frac{e^{-\frac{y^2}{q+2\sigma_y^2}}}{\left(q+2\sigma_y^2\right)^{3/2}}. \qquad (2.20)$$

An expression similar to eq. (2.20) can be derived for Δp_y.

2.2.2 Bassetti-Erskine formalism

Let us set

$$t^2 = \frac{q+2\sigma_y^2}{q+2\sigma_x^2}$$

in eq. (2.20), where t is another variable. After some algebra, one gets quantitatively, the x and y kicks experienced by an electron at a position (x, y) with respect to the origin centered at the passing positron bunch as

$$\Delta v_x = -\left(1-\frac{v_z}{c}\right)\frac{N_b e^2}{2\pi\varepsilon_0 m_e c}\int_r^1 dt\,\frac{x}{\sigma_x^2(1-r^2)}\,exp\left[-\frac{(1-t^2)\left(x^2+\frac{y^2}{t^2}\right)}{2\sigma_x^2(1-r^2)}\right], \quad (2.21a)$$

and

$$\Delta v_y = -\left(1-\frac{v_z}{c}\right)\frac{N_b e^2}{2\pi\varepsilon_0 m_e c}\int_r^1 dt\,\frac{y/t^2}{\sigma_x^2(1-r^2)}\,exp\left[-\frac{(1-t^2)\left(x^2+\frac{y^2}{t^2}\right)}{2\sigma_x^2(1-r^2)}\right], \quad (2.21b)$$

where σ_x and σ_y are the x and y standard deviations of the size of the bunch respectively, $r = \sigma_y/\sigma_x$ (assuming $\sigma_y < \sigma_x$), N_b the positron bunch population, v_z is the velocity of an electron in the EC before kick, m_e is the test-mass of the electron, and c is the velocity of light.

We combine the two expressions, given by eqs. (2.21a) and (2.21b), into one by introducing a complex error function as

$$\begin{aligned}\Delta v_x - i\,\Delta v_y = N_b\sqrt{A}\,\frac{e^2}{2\sqrt{\pi}\;\varepsilon_0\,c\,m_e}\Big[&\Big(Im\{W(-\sqrt{A}\,x - i\sqrt{A}\,y)\} - F\\ &\times Im\left\{W\left(-\sqrt{A}\,x\,r - i\sqrt{A}\,\frac{y}{r}\right)\right\}\Big)\\ &+ i\,\Big(Re\{W(-\sqrt{A}\,x - i\sqrt{A}\,y)\} - F\\ &\times Re\left\{W\left(-\sqrt{A}\,x\,r - i\sqrt{A}\,\frac{y}{r}\right)\right\}\Big)\Big], \end{aligned} \quad (2.22)$$

where

$$A = \frac{1}{2\sigma_x^2\,(1-r^2)},$$

$$F\exp\left[A\left(x^2r^2 + y^2 - x^2 - \frac{y^2}{r^2}\right)\right],$$

and, W, the complex error-function is

$$W(z) = e^{-z^2}\left(1 + \frac{2\,i}{\sqrt{\pi}}\int_0^z d\xi\, e^{\xi^2}\right),$$

where $z = \alpha + i\beta$. Comparing the real part of both the sides of eq. (2.22) gives the x-kick and that the imaginary part gives the y-kick. A computer program for the evaluation of W(z) was borrowed from CERN program library (in Fortran) [78] and was converted to C language [79].

The beam-kick to an electron is primarily in the x-y plane, however, an expression for a z-kick, which is similar to eq. (2.22) and much smaller than the x and y kicks, can be written as

$$\Delta v_z = \frac{N_b}{c}\sqrt{A}\frac{e^2}{2\sqrt{\pi}\varepsilon_0 c m_e}\Big[v_x\Big(Im\{W(-\sqrt{A}x - i\sqrt{A}y)\} - F \times Im\Big\{W(-\sqrt{A}xr - i\sqrt{A}\frac{y}{r})\Big\}\Big) + v_y\big(Re\{W(-\sqrt{A}x - i\sqrt{A}y)\}\big) - F \times Re\Big\{W(-\sqrt{A}xr - i\sqrt{A}\frac{y}{r})\Big\}\Big]. \quad (2.23)$$

The expressions in eqs. (2.22) and (2.23) use the electric fields that do not consider the boundary condition on the chamber wall. The beam-kicks, reduced to the well-known Bassetti-Erskine formula [76], are therefore approximately valid in our simulation model.

2.3 Generation of secondary electrons

An electron, originating at one end of the chamber wall, hits the opposite end with an increased kinetic energy and is lost. Depending on its angle of incidence and

the surface properties, it may generate one, more than one, or no electrons, usually referred as secondaries. Fig. 2.5 shows a schematic drawing of a collision of an electron with a surface, defined as an event, producing n secondaries with different energies. Electron multiplication on the chamber wall is a key contributor to the EC build-up.

It is parameterized by a secondary emission yield (SEY) of the chamber surface-wall. SEY, usually represented by δ, is defined as a ratio of the emitted secondary electrons per incident electron

$$\delta = \frac{I_s}{I_0}, \tag{2.24}$$

where I_s is the measured emitted electron current from the surface and I_0 is the incident electron beam current. The yield is a function of kinetic energy E_0 of the incident electron beam, its incident angle θ_0 with respect to the inner normal of the surface, i.e., $\delta = f(E_0, \theta_0)$, the type of surface material and its state of conditioning.

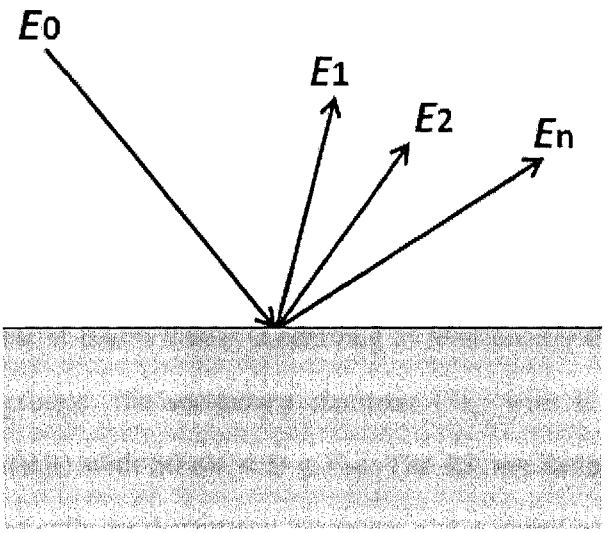

Fig. 2.5. In an "event", a single electron (with energy E_0) strikes a surface and yields 'n' secondaries with energies E_1, E_2, ... E_n.

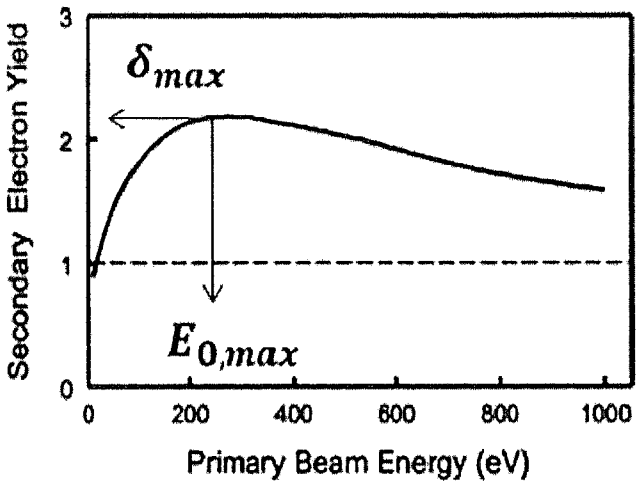

Fig. 2.6. SEY of alkali-etched Al alloy vs. primary electron energy E_0.

The average number of secondaries per incident electron is described by a universal curve (Fig. 2.6), which is characterized by only two material parameters: the maximum SEY for normal incidence, δ_{max}, which is defined as $\delta_{max} = f(E_{0,max},0)$, and the energy at which this maximum occurs. From the Fig. 2.6, it is evident that δ_{max} occurs at $E_0 = 295$ eV for alkali-etched aluminum alloy [80].

2.3.1 Probabilistic description of secondary emission

If a surface is bombarded with primary electrons (PE), electrons are released. Fig. 2.7 shows schematically the energy distribution of these electrons released by PE with energies 100 eV < E_{PE} < 1 keV. According to their energy the electrons can be divided into two groups: the secondary electrons (SE) with E ≤ 50 eV and the reflected electrons (RE) with 50 eV < E ≤ E_{PE}. The RE are further classified into a narrow peaked elastically backscattered electrons and a broad zone of inelastically backscattered electrons. Superimposed on the energy distribution are Auger electrons having an energy depending on the surface material. The SE yield is up to 10^4 times

higher than the Auger electron yield [71]. There is no fundamental distinction between SE and RE; however, it is advantageous for the purposes of phenomenological fits, to treat them separately. At the quantum level, of course, this distinction is unphysical.

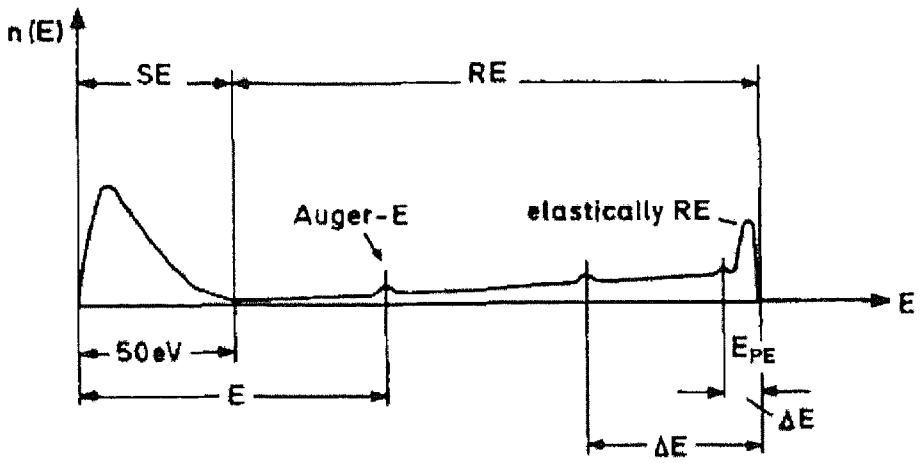

Fig. 2.7. Schematic energy distribution of electrons which are emitted from a surface bombarded with PE [71].

We adopted the Furman-Pivi model for the generation of secondary emission [81]. The input ingredients of the model are the measured data for SEY, i.e., δ and the emitted-energy spectrum, i.e., $d\delta/dE$ of the secondary electrons. Consider an event of electron-surface collision, which generates n electrons with kinetic energies E_1, E_2, ...E_n. The directions of all the emitted electrons, given by (θ_1, ϕ_1), (θ_2, ϕ_2), ...(θ_n, ϕ_n) are uncorrelated. Furman and Pivi developed the most differential probability, i.e. the joint probability for n electrons ($0 \leq n \leq 10$) to be emitted with kinetic energies E_1, E_2,.... E_n into the solid angles Ω_1=(θ_1, ϕ_1), Ω_2=(θ_2, ϕ_2),... and Ω_n=(θ_n, ϕ_n) when a primary electron strikes the chamber wall at a given incident energy E_0 and an angle θ_0. The joint probability, represented by, $\mathcal{P}_n(E_1, E_2, \ldots\ldots E_n, \Omega_1, \Omega_2, \ldots\ldots\ldots \Omega_n)$, is expressed in its most general form as

$$\mathcal{P}_n = \frac{dP_n}{dE1\ d\Omega1\ \ dE2\ d\Omega2\ \ldots..dEn\ d\Omega n}. \qquad (2.25)$$

The probability P_n that in an event n electrons will be emitted with arbitrary energies and directions for a fixed E_0 and θ_0 is obtained by integrating $\mathcal{P}_n$ over the entire phase space of the secondary electrons and is expressed as

$$P_n(E_0, \theta_0) = \int (dE_1\ dE_2\ \ldots\ldots dE_n)(d\Omega_1\ d\Omega_2\ \ldots\ldots d\Omega_n)\ P_n. \qquad (2.26)$$

The P_n's obey the conditions $P_n \geq 0$, and $\int P_n$=1. The total SEY is the average electron multiplicity in an event and is given by

$$\delta(E_0, \theta_0) = \langle n \rangle \equiv \int_0^\infty n\ P_n. \qquad (2.27)$$

The emitted-energy spectrum is given as

$$\frac{d\delta}{dE} = \sum_n \int (dE_1\ dE_2 \ldots dE_n)(d\Omega_1\ d\Omega_2 \ldots d\Omega_n)\mathcal{P}_n \sum_{k=1}^{n} \delta_{Dirac}(E_k - E), \qquad (2.28)$$

where E_k is the energy of the k^{th} emitted electron in an event generating n secondaries.

2.3.2 Model of SEY

Conventionally, the definition of the three components associated with the SEY is based on the energies at which the secondaries are emitted [71, 82, 83]. As shown in the schematic (Fig. 2.8), they are

a) Elastically backscattered electrons at the wall surface I_{el}. These electrons are emitted with energy equal to the energy of the incident electron.

b) Rediffused electrons I_{rdf}, are the ones that are reflected out after being scattered from one or more atoms inside the bulk material.

c) True secondaries I_{ts} , which come from the primary electrons that penetrated a few tens of nanometers into the material. Their emission energy is a few eV.

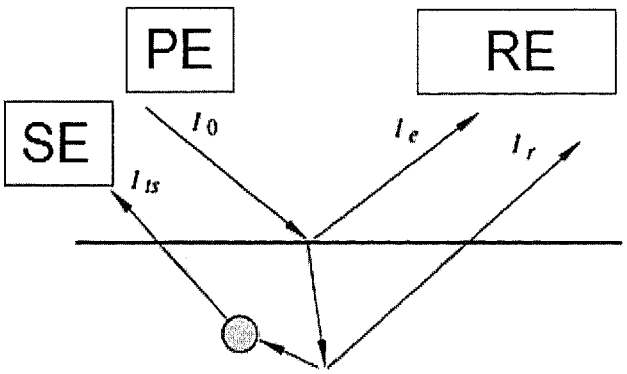

Fig. 2.8. Schematic of currents that are used to define three components of SEY.

The yields for each type of components are defined by $\delta_{el} = I_{el}/I_0$, $\delta_{rdf} = I_{rdf}/I_0$, and $\delta_{ts} = I_{ts}/I_0$, so that the total SEY is

$$\delta = \frac{I_{el} + I_{rdf} + I_{ts}}{I_0} = \delta_{el} + \delta_{rdf} + \delta_{ts}. \qquad (2.29)$$

However, there is no fundamental distinction between the backscattered and rediffused mechanism. In practice, there exists a conventional criterion [83, 84], that leads to this distinction, and hence to separate the measurements of δ_{el}, δ_{rdf}, and δ_{ts}.

2.3.3 Mutual-exclusion assumption for SEY components

Assigning the three components of δs to the P_n s is based on the assumption that the elastic and rediffused electrons are only produced in one-electron events (n = 1), while the true-secondary electrons are produced in events with any number of secondary-electrons ($n \geq 1$). This means that in any given event backscattered and rediffused electrons are never accompanied by true-secondaries, and, conversely, when two or more true-secondaries are produced, they are never accompanied by either backscattered or rediffused electrons.

Following this assumption, the three δs can therefore be related to P_n s by

$$\delta_{el} = P_{1,el},$$

$$\delta_{rdf} = P_{1,rdf},$$

$$\delta_{ts} = P_{1,ts} + \sum_{n=2}^{\infty} P_{n,ts}. \qquad (2.30)$$

In terms of f_n's, the energy distribution functions, we can write

$$f_1 = f_{1,el} + f_{1,rdf} + f_{1,ts},$$

$$f_n = f_{1,ts}, \quad n \geq 2. \qquad (2.31)$$

For emission angles of n secondaries, we adopted the experimental fact [84] that the true-secondary electrons have $cos\theta$ angular distribution, which is fairly independent of the primary incident angle θ_0 and incident energy E_0. The elastically scattered and rediffused electrons have a complicated angular distribution; however, in our simulation model we followed the same emission-angle distribution for all electrons, regardless of the physical mechanism by which they are generated.

2.3.4 Model of SEY for true-secondary electrons

The SEY is dominated by the true-secondaries at low incident energies ($E_0 \leq 40$ eV). The energy and the angular dependence of δ_{ts} were fitted experimentally [71, 82, 84] as

$$\delta_{ts}(E_0, \theta_0) = \hat{\delta}(\theta_0)\, D\left[E_0/\hat{E}(\theta_0)\right], \tag{2.32}$$

where D(x), an approximately universal scaling function, is

$$D(x) = \frac{sx}{s - 1 + x^s}. \tag{2.33}$$

The fitting parameters for copper surface at normal incidence ($\theta_0 = 0$) are: $\hat{\delta}(0) = 1.8848$, $\hat{E}(0) = 276.8$ eV and $s = 1.54$.

2.3.5 Model of SEY for elastically scattered electrons

Following the experimental data [83, 84], the incident-angle dependent $\delta_{el}(E_0,\theta_0)$ can be represented by

$$\delta_{el}(E_0, \theta_0) = \delta_{el}(E_0, 0)[1 + e_1(1 - cos^{e_2}\theta_0)], \tag{2.34}$$

where

$$\delta_{el}(E_0, 0) = P_{1,e}(\infty) + \left[\hat{P}_{1,e} - P_{1,e}(\infty)\right] \frac{exp\left(-\frac{|E_0 - \hat{E}_e|}{W}\right)^p}{p},$$

and, where the fitting parameters for copper surface at normal incidence ($\theta_0 = 0$) are: $P_{1,e}(\infty) = 0.02$, $\hat{P}_{1,e} = 0.496$, $\hat{E}_e = 0$ eV, $W = 60.86$ eV, $p = 1$, $e_1 = 0.26$ and $e_2 = 2$.

2.3.6 Model of SEY for rediffused electrons

Following the experimental the experimental data [83, 84] once again, the incident-angle dependent $\delta_{rdf}(E_0,\theta_0)$ can be represented by

$$\delta_{rdf}(E_0,\theta_0) = \delta_{rdf}(E_0,0)[1 + r_1(1 - cos^{r_2}\theta_0)], \quad (2.35)$$

where

$$\delta_{rdf}(E_0,0) = P_{1,r}(\infty)\,[1 - exp(-(E_0 - E_r)^r)].$$

The fitting parameters for copper surface at normal incidence ($\theta_0 = 0$) are: $P_{1,r}(\infty) = 0.2$, $E_r = 0.041$ eV, $r = 0.104$, $q = 0.5$, $r_1 = 0.26$ and $r_2 = 2$.

2.3.7 Model for the emission probabilities of true-secondaries

We chose a binomial distribution for $P_{n,ts}$ given by

$$P_{n,ts} = {}^{M}C_n\, p_n\, (1-p)^{M-n}, \quad (2.36)$$

where $p = \langle n \rangle / M = \delta_{ts}/M$ and $0 \leq n \leq M$. In our simulation we chose $M = 10$, which means that this distribution limits the number of emitted secondary electrons to a maximum of 10. This limitation is not physical. However, it is sufficient for all the materials.

2.3.8 Comparison of fits to the experimental data

The emitted-energy spectrum, $d\delta/dE$, is modeled through f_n's, the energy distribution functions for the emitted electrons by fitting parameters (ref. [81] and the references there in). The mathematically self-consistent phenomenological probabilistic model for the secondary-emission process ensures that the four input quantities (3 δ's and $d\delta/dE$) are recovered upon statistical average over a large number of events. The abovementioned fitting parameters correspond to a δ_{max} = 2.0817 for a chemically cleaned copper but not *in situ* vacuum-baked sample.

Based on the algorithm for photoelectron generation as mentioned in sec. 2.1 and the Furman-Pivi [81] algorithm for secondary electron generation, we developed a code to benchmark the P_n's and dδ/dE, the emitted-energy spectrum.

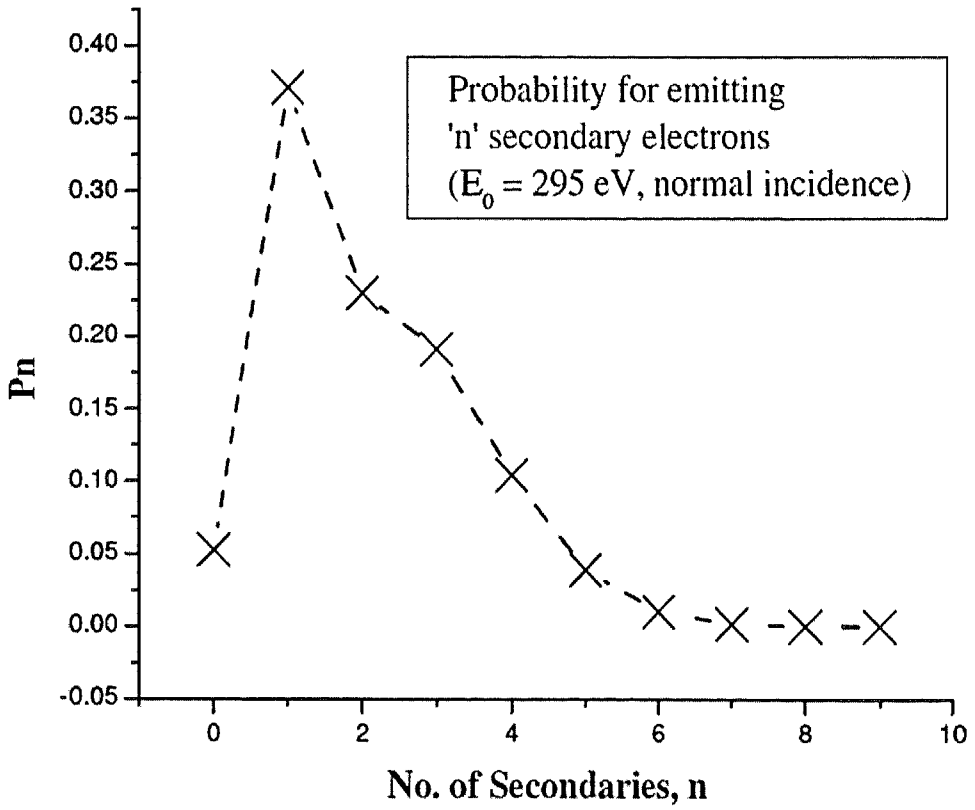

Fig. 2.9. Probability distribution of 10 secondary electrons emission.

For benchmarking the P_n's, we started with 5 million electrons in a test simulation, all at 295 eV energy striking the copper surface at normal incidence. The plot in Fig. 2.9 shows a probability distribution for an emission of a maximum of ten secondary electrons. The result matched exactly with Furman-Pivi [81] model.

For benchmarking the emitted-energy spectrum, we started with 100,000 electrons in next test simulation, all at 295 eV energy striking the copper surface at normal incidence.

Fig. 2.10 shows the contributions of the three components of δ, when an electron beam (E_0 = 295 eV) impinges on a copper surface. The $d\delta/dE$ spectrum from the simulations matched quite well with the experimental data [85].

For benchmarking the SEY, we started with 50,000 electrons in another test simulation, with energy 0 eV $\leq E_0 \leq$ 1400 eV, striking perpendicular to the copper surface.

Fig. 2.11 shows a plot of SEY as a function of incident electron energy normal to the surface. The maximum SEY occurs at an energy E_0 = 295 eV of the incident electron as expected. A fluctuation in the plot is also observed at E_0 = 200eV, which is speculated to be due to poor statistics, and this diminished with an increase in the number of test electrons in our simulation.

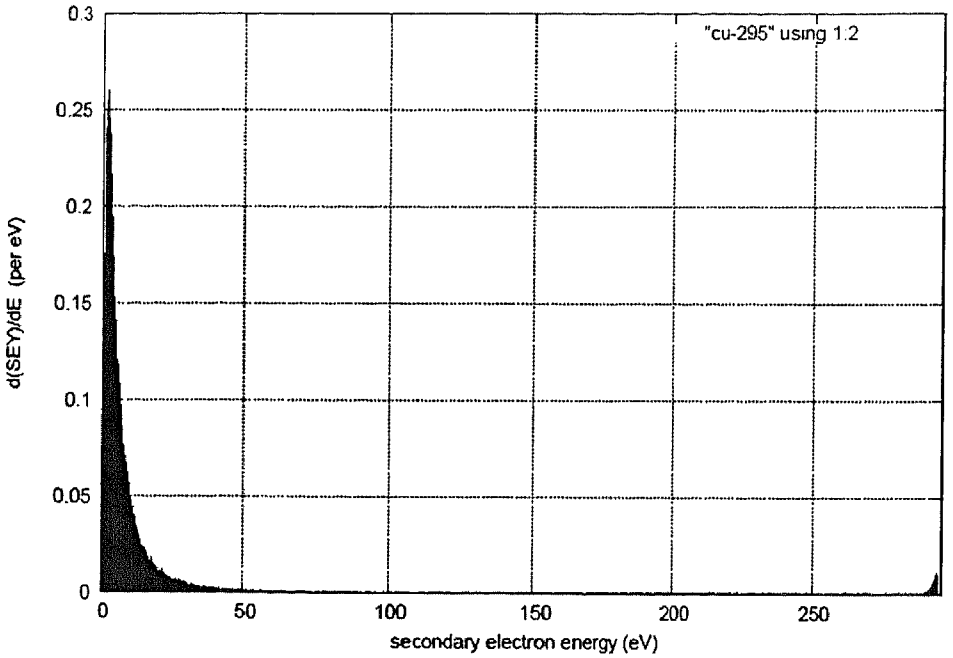

Fig. 2.10. Emitted-energy spectrum for copper at 295 *eV* incident energy and normal incidence on chemically cleaned but not *in situ* vacuum-baked samples.

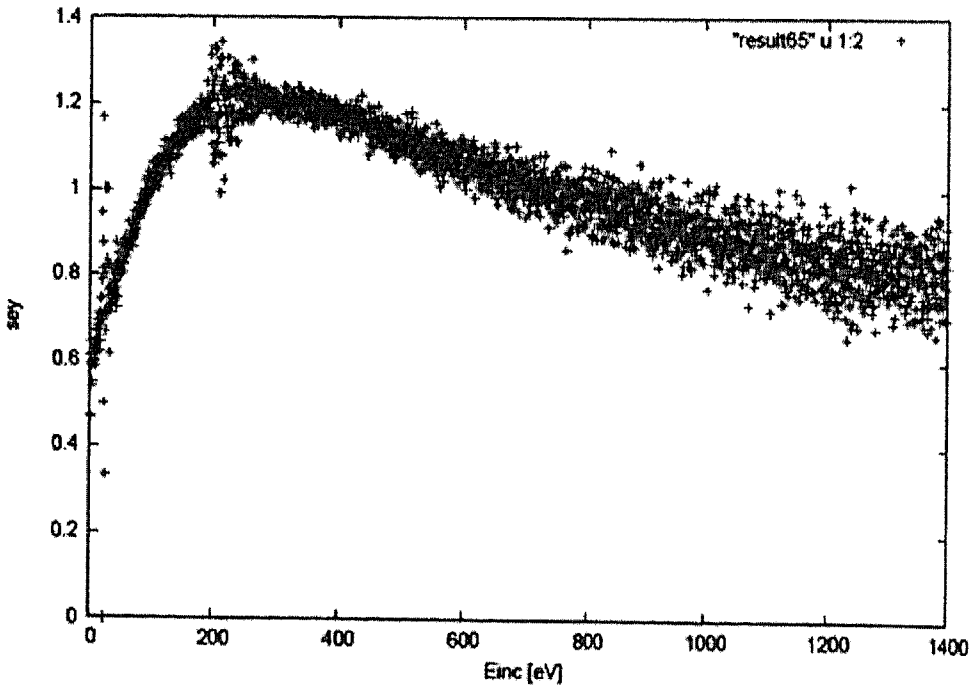

Fig. 2.11. The SEY for copper at 295 *eV* normal incidence.

2.4 EC-space charge calculation

Previously we showed how the primary electrons are created (sec. 2.1.1), accelerated to the beam pipe due to electron-beam interaction (sec. 2.2.2), and multipactored by the secondary emission (sec. 2.3). However, the phenomenon of the electron multiplication does not continue forever. When there is a sufficient accumulation of the electrons inside the beam chamber, the electric potential due to space charge of the EC balances the beam potential and restricts the secondary electrons from being attracted by the beam, thus stopping them to collide with the chamber wall for further multiplication.

To calculate the electric fields produced by the electrons inside the chamber, we numerically solve the Poisson's equation for the electrostatic potential of the EC. The Poisson's equation is

$$\nabla^2 u(x,y) = -\frac{\rho(x,y)}{\varepsilon_0}, \qquad (2.37)$$

where $u(x,y)$ is the electrostatic potential of the EC. We represent '$-\rho/\varepsilon_0$' by 'f'. In its discrete form the Poisson's equation can be expressed as

$$u_{i-1,j} + u_{i+1,j} + u_{i,j-1} + u_{i,j+1} - 4\,u_{i,j} = h^2 f_{i,j}\,, \qquad (2.38)$$

where $u_{i,j}$ represents the electrostatic potential, and, $f_{i,j}$ the source-term, in the ith row and the jth column on a square grid of size h. The $u_{i,j}$'s were solved by the alternating direction implicit (ADI) method, an iterative technique [86].

The procedure of the ADI is as follows:

a) Assume any value of $u_{i,j}$, for example 0 (since at any metallic boundary the potential is zero, a Dirichilet boundary condition), and solve it for a fixed row as

$$u_{i,j-1} - 4u_{i,j} + u_{i,j+1} = h^2 f_{i,j} - u_{i-1,j} - u_{i+1,j}.$$

Repeat the step a) for all rows.

b) Solve for $u_{i,j}$ with modified values for a fixed column as

$$u_{i-1,j} - 4u_{i,j} + u_{i+1,j} = h^2 f_{i,j} - u_{i,j-1} - u_{i,j+1}.$$

Repeat the step b) for all columns.

c) Steps a) and b) resulted in a band matrix, which were solved by Gauss-Elimination method.

d) Steps a) to c) were repeated till $u_{i,j}$'s converged.

The EC is built up inside a 3-dimensional cylindrical volume of the beam-pipe. Once it is saturated, it can be approximated to have a uniform longitudinal distribution i.e. along the z-axis in a field-free (drift space) region. Under this approximation, it is therefore justified to solve for a 2-D potential $u(x,y)$ instead for a 3-D potential $u(x,y,z)$.

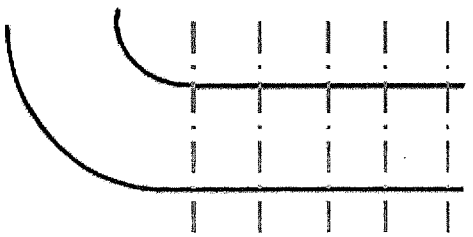

Fig. 2.12. The CBX was longitudinally divided into 4 zones for space charge calculations. '*h*', the mesh size was chosen as 4.7 *mm*.

As shown in Fig. 2.12, we divided the CBX into four equal zones in our simulations. Based on the *z*-coordinate of each macro-electron, they were assigned a zone. In a given zone all the electrons were assumed to be located in one transverse plane

bounded by a metallic boundary of the beam-pipe. Each of the four zones were divided into identical square meshes (0.47 m × 0.47 m) for the calculation of $u_{i,j}$'s on each mesh point of that zone. At the boundary of the beam-pipe the discrete form of the 2-D Poisson equation is modified as

$$\nabla^2 u_0 \approx \frac{2}{h^2}\left[\frac{u_A}{a(a+p)} + \frac{u_B}{b(b+q)} + \frac{u_P}{p(p+a)} + \frac{u_Q}{q(q+b)} - \frac{ap+bq}{abpq}\,u_0\right],$$

where a, b, p and q are the fractions (Fig. 2.13) of the mesh size.

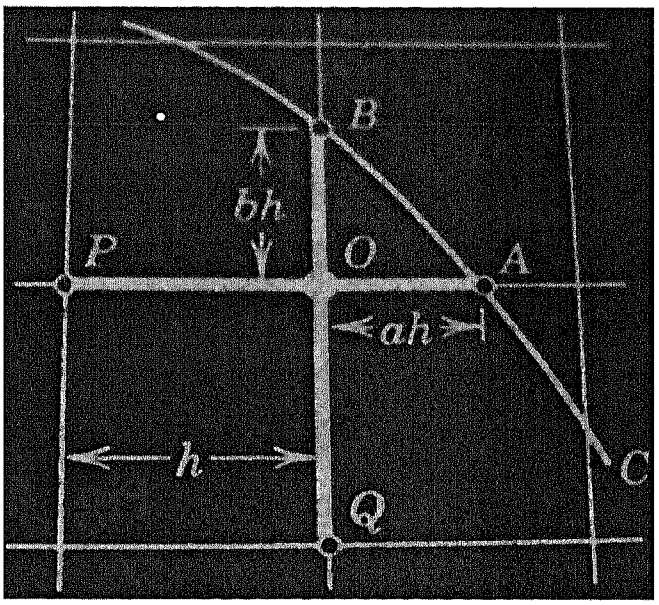

Fig. 2.13. Schematic of fractional mesh lengths near an arbitrary boundary point O for the calculation of the modified potential. Both a and b are less than unity.

For space charge force calculations, electric fields $\{E_x(x, y), E_y(x, y)\}$ need to be calculated at the position of each electron. We followed the steps, mentioned below, to calculate the electric fields

a) *Charge deposition*: Place charges on a numerical grid.

b) *Field Solution*: Solve for u_{ij}'s from ADI. The equivalent electric fields at numeric grids are calculated from

$$E_{i,j}^{x} = -\frac{u_{i,j-1} - u_{i,j+1}}{2h},$$

$$E_{i,j}^{y} = -\frac{u_{i-1,j} - u_{i+1,j}}{2h}.$$

c) *Field Interpolation*: Interpolate the fields at the positions of the macro-electrons based on the field values at the grid locations.

For the charge assignment $\rho_{i,j}$ on each mesh point (i,j) of a given zone, we quantized the charge density ρ (x, y). We followed cloud-in-cell (CIC) scheme, a popular particle-in-cell approach for the electrostatic problems [87]. In 2-D CIC scheme, the charge associated with a given charged particle is deposited on four mesh points that make up the vertices of a square surrounding that particle. The amount of charge deposited on each vertex is called the weight, and the sum of all the weights is unity. The same weights were used during the interpolation phase to compute the interpolated field value at the particle positions.

The simulations showed that the magnetic field carried by the moving EC is ~ 10^{-9} T. The contribution of v×B term to the space-charge force was < 10^{-6} N/coulomb, a value that is negligible compared to that contributed by the electric field. It is therefore justified to consider only the scalar potential to calculate the space charge field of the EC.

2.5 EC tracking

In sec. 2.1.1, we defined a macro-electron and a simulation parameter viz. *ftf*, which is not known a priori. In our simulations, we kept it as 405 to get a good statistics of macro-electrons entering the RFA entrance once the EC build-up gets saturated. With *ftf* = 405, there are ~10,000 macro-photoelectrons generated per bunch pass in the CBX length.

The generation of the photoelectrons depends on the bunch population. For easiness in mathematical modeling, the bunch was assumed to have a 3-D Gaussian profile. Therefore, the number of the photoelectrons per unit bunch-length, generated at the pipe-wall inside the CBX, is non-uniform. In simulations, the bunch-length is usually divided into a number of slices so that the photoelectron generation per unit bunch-slice-length can be approximated to a uniform. In our code, we divided the bunch-length into ten slices. There is bunch separation of 6 ns in KEKB LER; accordingly, the bunch gaps were also sliced longitudinally, typically into 550 slices. A bunch-slice-length and a gap-slice-length, so chosen, are equal, each representing a time-step of approximately 4.7 *ps*, which is a time step of the simulation when bunch slices stay in the CBX (Fig. 2.14).

The one-meter-long CBX is divided into an integral number of cells such that each cell-length is equivalent to 4.7 *ps*. The electron is tracked for every 4.7 *ps* in each cell-length. We followed the below mentioned steps for the tracking of a macro-electron:

a) The position of each bunch-slice entering the CBX was recorded at every time-step. For instance, two bunch slices in the CBX at time step 2 are shown in Fig. 2.15, where the slice # I is in cell # 2 and slice # II is in cell # 1, each generating macro-photoelectrons in respective cells.

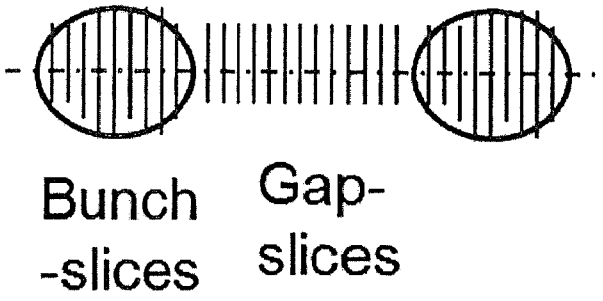

Fig. 2.14. Schematic of bunch-slices and intra bunch gap-slices.

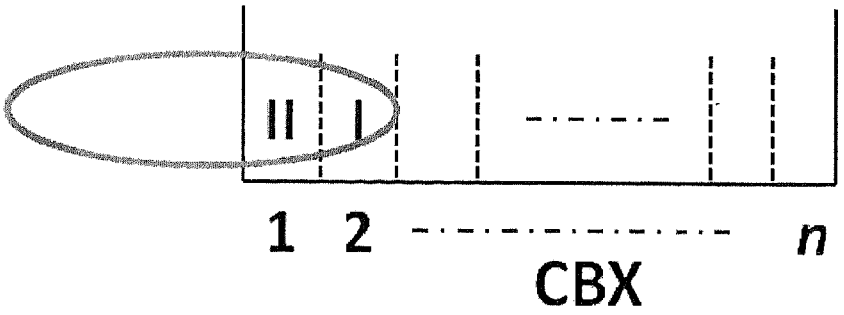

Fig. 2.15. At t=2 bunch slice # I and # II are in the first two cells of the CBX.

b) Each bunch-slice generates macro-photoelectrons in a CBX-cell occupied by it. The slice imparts a kick to only those macro-electrons that share the same CBX-cell. The rest of them continue drifting in the CBX with unchanged velocities.

c) While tracking, the macro-electrons might leave the CBX at any instant before hitting the wall. To maintain the continuity of the electron flow, they were made to reappear in the next time-step with the same transverse position and energy at the other end of the CBX.

At any instant the velocity of a macro-electron changes depending on whether it received a kick by a bunch-slice. The space charge calculation, done at every bunch pass, gives the electric field that is experienced by the macro-electrons at their

respective locations. Knowing the initial position and velocity of each macro-electron, the force-equations $m_e\ddot{x} = -e\,E_x(x,y)$, $m_e\ddot{y} = -e\,E_y(x,y)$ and $m_e\ddot{z} = 0$ were solved numerically. We implemented a 3-D 4th-order Runge-Kutta algorithm [88] in our code to solve the coupled second-order differential equations. The resulting new set of position and velocity viz. (x, y, z, v_x, v_y, v_z) is used to replace with the previous set for each macro-electron. The electrons are tracked at every time-step following the same procedure.

2.6 Buffer management

All the macro-electrons, originating at one end of the beam-pipe, drift towards the other end while being tracked inside the CBX. When it collides with the beam-pipe, it is lost and generates secondary electrons there. At any time-step some macro-electrons are lost, some are born as secondaries, while a fixed number of them are always generated as macro-photoelectrons due to the incoming bunches. The phenomenon continues at every time-step. As a result, the total number of macro-electrons inside the CBX keeps changing at every time-step.

In simulations, the IDs of the macro-electrons (viz. its positions and velocities) are stored in an array. An array of seven million size was kept as the main-buffer in our code to store the position (x_i, y_i, z_i) and velocity (vx_i, vy_i, vz_i) of the macro-electrons. The IDs of all the electrons that are lost to the pipe-wall were stored in another array, which we defined as the garbage-buffer. The size of the garbage-buffer-array was kept as 30,000 in our code. The electrons that are lost must not be tracked again in simulations. To accomplish this, we developed an efficient buffer management technique, the procedure of which is mentioned in the following steps:

a) The IDs of all the macro-electrons, which hit the chamber wall, are stored in the garbage-buffer.
b) Starting from the top-filled slot in the main-buffer, the survived electrons are shifted to the emptied slots by the lost electrons. This results in an arrangement of the survived electrons occupying the slots of the main-buffer from bottom to top in a continuous manner.
c) The secondary electrons generated at that time-step are placed in the newly arranged main-buffer over the top-filled slot.
d) The number of the macro-electrons, which are to be tracked in the next time-step, is modified.
e) The garbage-buffer containing the IDs of the lost electrons at that time-step is cleared.

The same procedure of the buffer management is followed when electrons are lost at the chamber wall during bunch-slices or gap-slices in the CBX at any time-step.

2.7 Benchmarking of code

The first benchmarking of our code was done with a pioneer work by K. Ohmi [28]. The plot in Fig. 2.16a shows a transient distribution of the photoelectrons after 27 bunch passes for KEK photon factory (PF) ring parameters.

The plot in Fig. 2.16b shows our simulation results for the same beam parameters. The difference in the plots is due to a 3-D velocity distribution of macro-electrons consideration in our code.

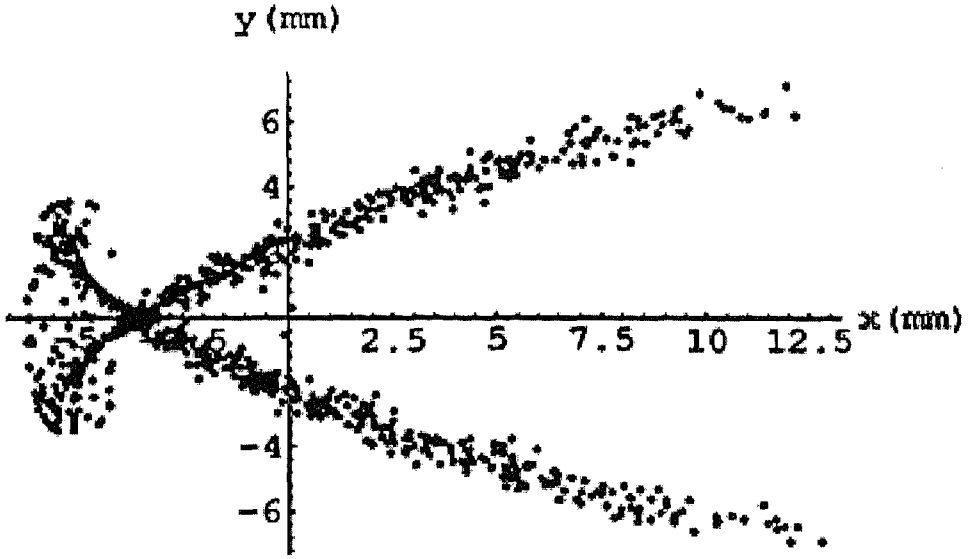

Fig. 2.16a. Ohmi's result of an x-y distribution of the photoelectrons after 27 bunch-passes [28].

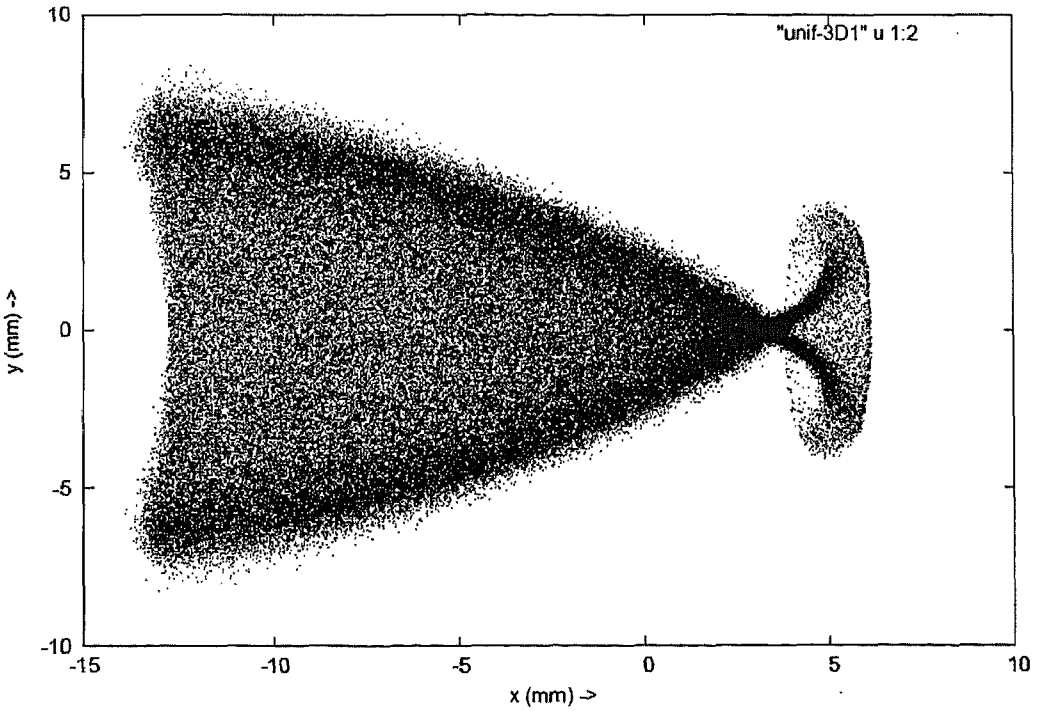

Fig. 2.16b. x-y distribution of the photoelectrons from our code after 27 bunch-passes.

For testing of our code, we chose $\delta_{max} = 1.2$, $i_B = 1\ mA$ and a bunch train of 200. Fig. 2.17 shows the EC build-up, resulted from our code, as a function of the number of bunch passes.

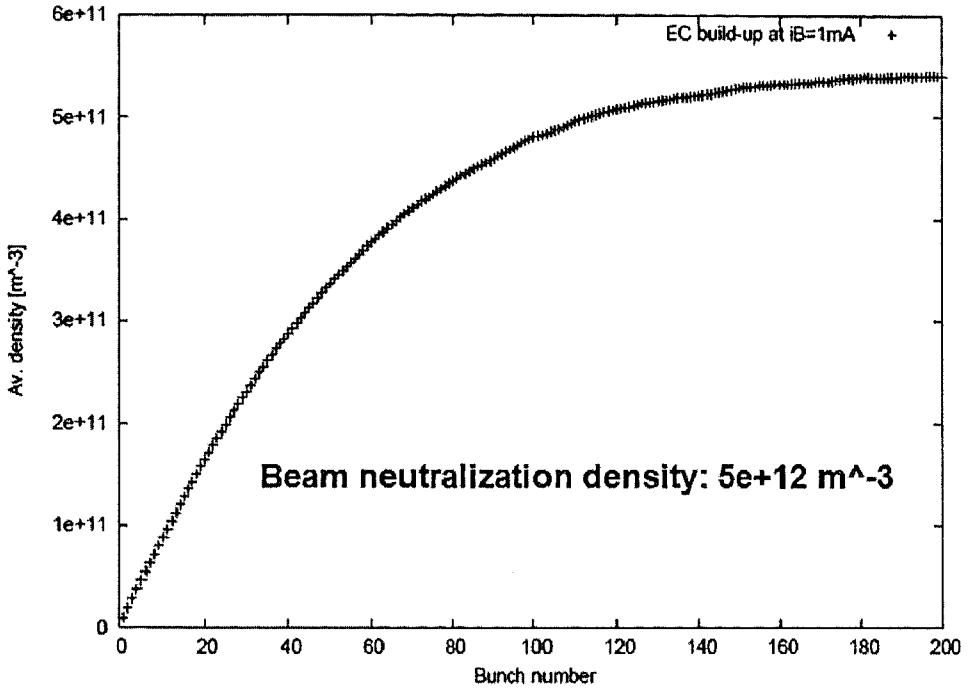

Fig. 2.17. EC build-up from our code. The average density of macro-electrons (y-axis) saturates after 180 bunch passes (x-axis).

The total charge of 1 *mA* positron bunch moving with 99.4 *kHz* revolution rate is ~ 10 *nC*. The volume occupied by a positron bunch inside the chamber, before arrival of the next bunch, is $\pi r_{chm}^2 L_{bunch}$, i.e., 0.0125 m^3. Therefore, the positron bunch neutralization density inside the KEKB LER chamber is ~ 5×10^{12} m^{-3}. The saturation density of the EC from our simulations is ~ 5.3×10^{11} m^{-3}, an order of magnitude less than the beam neutralization density, thereby suggesting that for $\delta_{max} = 1.2$, the number of electrons that are lost to the wall is quite high.

A 3-D snapshot of x-y distribution of the macro-electrons, resulting from our code, is shown in Fig. 2.18 for the same simulation conditions as mentioned above, at the end of 200 bunch passes.

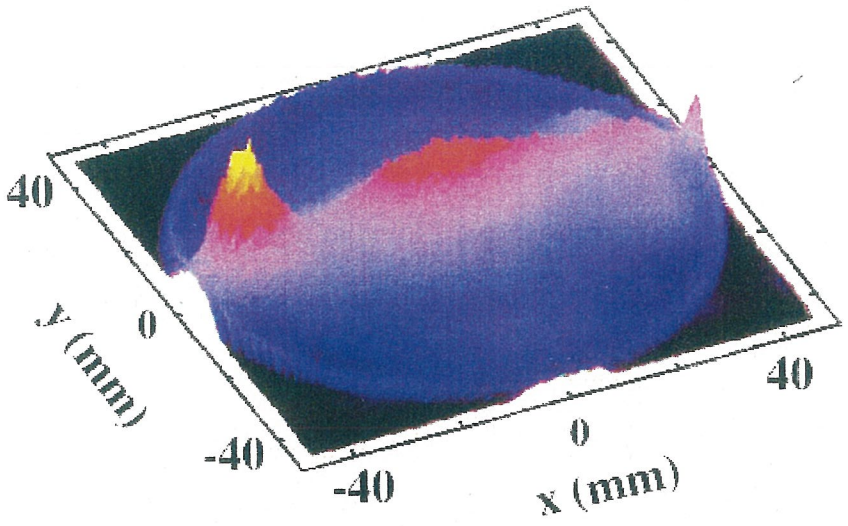

Fig. 2.18. A 3-D snapshot of transverse distribution of the EC after 200 bunch passes. $\delta_{max} = 1.2$, $i_B = 1\ mA$.

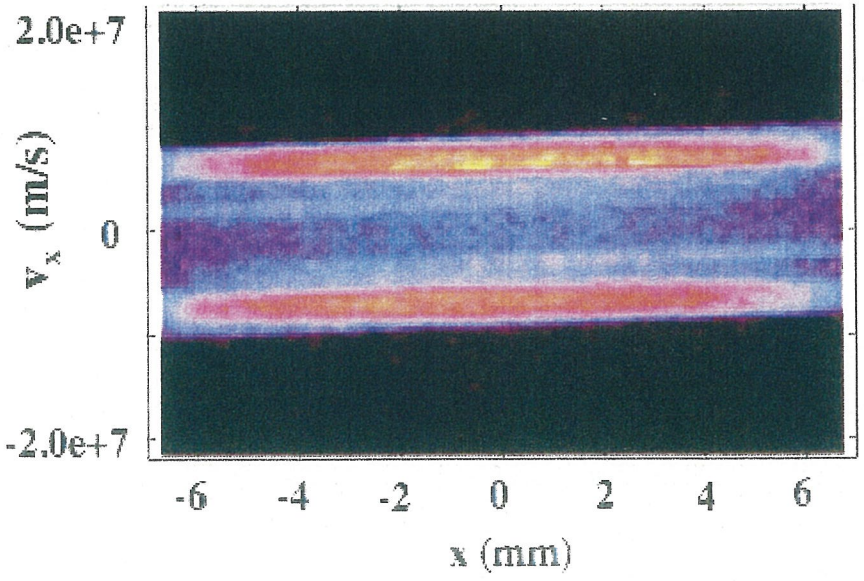

Fig. 2.19. x-v_x phase space distribution of the macro-electrons after 200 bunch passes. $\delta_{max} = 1.2$, $i_B = 1\ mA$.

Fig. 2.19 shows a x-v_x phase space distribution of the macro-electrons resulted from our code after 200 bunch passes. The range of the x-component of the velocity of the macro-electrons is $\pm 8\times10^6$ m/s within a radius of ~7 mm around the beam.

Similarly a y-v_y phase space distribution shows that the range of the y-component of the velocity of the macro-electrons is $\pm 4\times10^6$ m/s within a radius of ~7 mm around the beam.

Fig. 2.20 shows a potential distribution (V(x,0) vs. x) of the EC at an arbitrarily chosen z, resulted from our code after 200 bunch passes. The horizontal axis is the radial distance across the beam-chamber diameter (-47 *mm* ≤ x ≤ 47 *mm*; y=0 *mm*) and the vertical axis is the potential due to space charge of the EC.

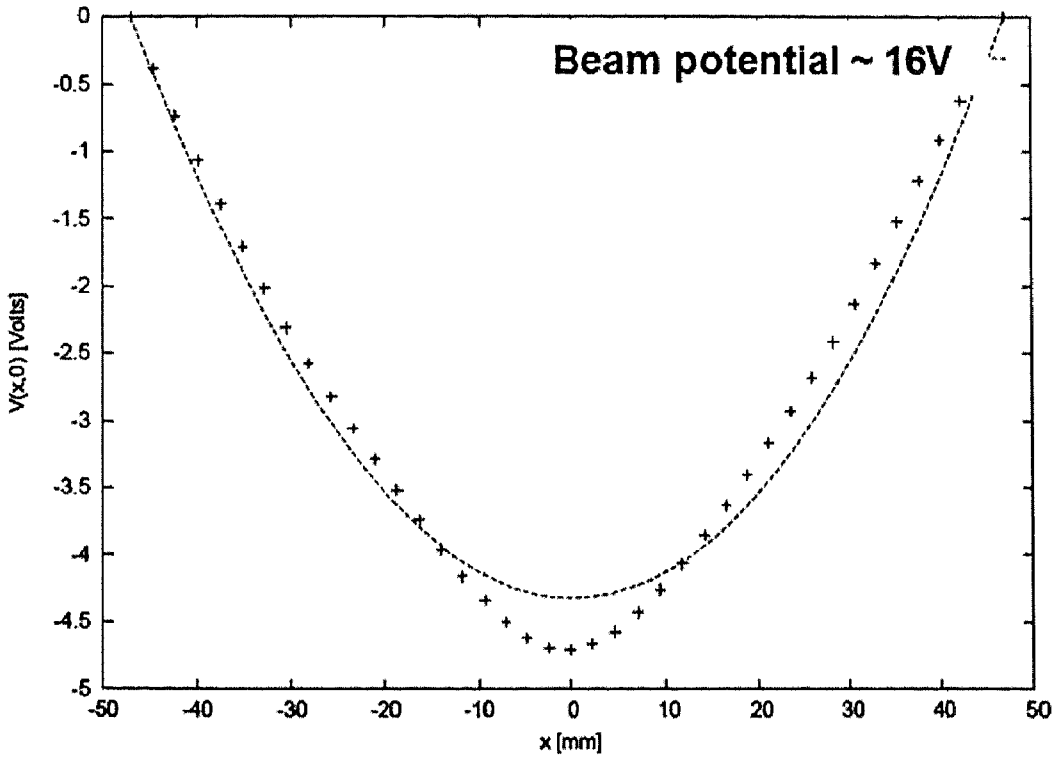

Fig. 2.20. V(x,0) vs. x after 200 bunch passes. $\delta_{max} = 1.2$, $i_B = 1$ *mA*.

If the EC is assumed to be uniformly distributed inside the beam-pipe over the CBX length, then analytically, the electrostatic potential inside a metallic cylinder with a uniform charge distribution is given by

$$V(r) = \frac{\rho}{4\pi\varepsilon_0}(r_{chm}^2 - r^2),$$

where r is the distance from the center of beam-pipe at which the potential is to be calculated. Simulations revealed that after 200 bunch passes the average charge density inside the beam-chamber is $\rho \sim -54.4\ nC/m^3$. The potential distribution by analytic estimate is shown by dotted lines and that by simulations is shown by symbol '+' in Fig. 2.20. The two curves match quite significantly; for instance the analytic estimate of V(r) at $r = 0$ is - 4.33 *Volts* and that by simulations is - 4.7 *Volts*. The beam potential is ~ 16 *Volts*, suggesting that the potential due to space charge of EC is quite weak at $\delta_{max} = 1.2$ and $i_B = 1\ mA$.

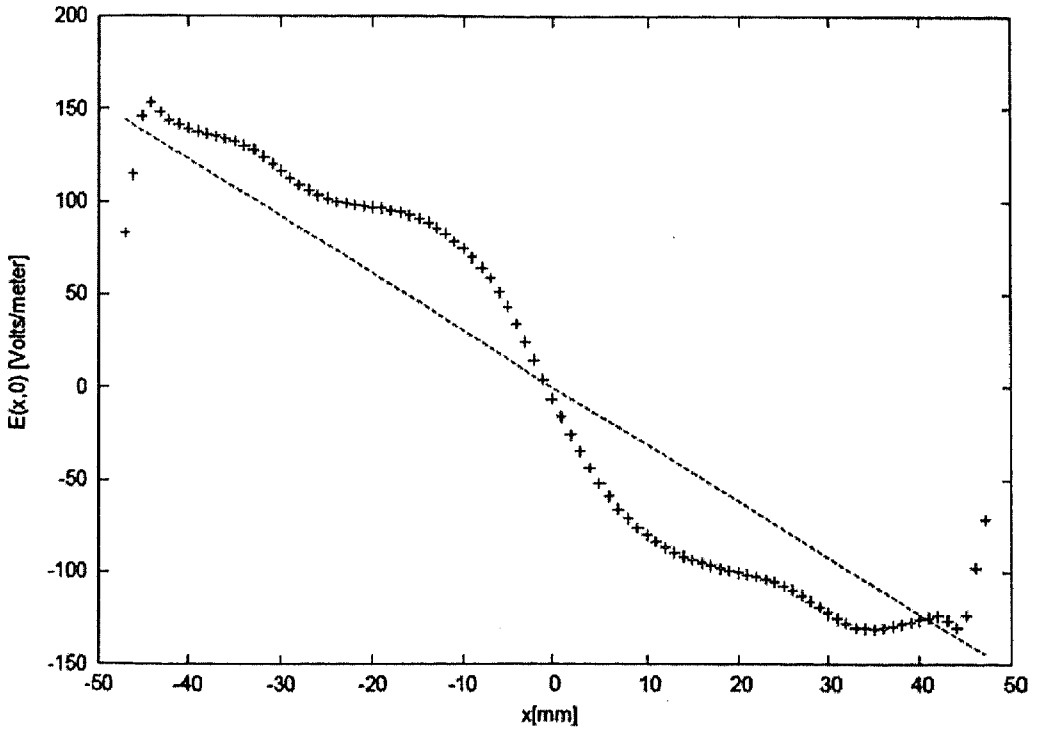

Fig. 2.21. E_x(x,0) vs. x after 200 bunch passes. $\delta_{max} = 1.2$, $i_B = 1\ mA$.

Fig. 2.21 shows a comparison of electric field due to space charge of the EC (shown with '+' symbol) with that by analytic estimate (shown with dotted line), the two curves match quite closely.

Chapter 3: ANALYSIS OF THE MEASUREMENT

In this chapter, we present the method of measurement, an analytic formalism to find the near-beam electron cloud density (ECD), modeling of the electron monitor to calculate the yield of macro-electrons, comparison of an observed volume occupied by the near-beam electrons in analytic formalism with that in simulations, comparison of the near-beam ECD by the experimental data and analytic formalism with that by the simulations, and finally the validity of the analytic formalism.

3.1 Method of the measurement

3.1.1 Measurement principle

Fig. 3.1 shows a schematic drawing of the electron monitor assembly installed in a drift region in KEKB LER [67]. The assembly consists of an anode for collecting the electrons and a retarding grid, which repels the electrons, whose energy is less than eV_b, where V_b is a bias voltage applied to the retarding grid.

Applying a bias potential to the retarding grid, e.g. -1 kV, one collects only those electrons at the anode whose energy is 1 keV or more. The electrons with energy equal to eV_b or above shall henceforth be referred as the "energetic electrons". The source of a high-energy component of the electrons is expected to have originated from a region near the beam because of a strong electron-beam interaction near the beam. Thus, the detection of the energetic electrons provides information of a region around the beam where they stayed at the time of interaction. This region around the beam defines a volume, which we call it as an observed volume (Fig. 3.2a). Experimentally, one measures the current of the energetic electrons at the electron

monitor, and hence the number of energetic electrons, by using a retarding field analyzer (RFA) located on the chamber wall. Therefore, for the estimation of near-beam ECD, the calculation of the observed volume is very essential. A unique feature of the method is that it measures the density of the electrons as seen by the beam. It has also an advantage of being non-destructive.

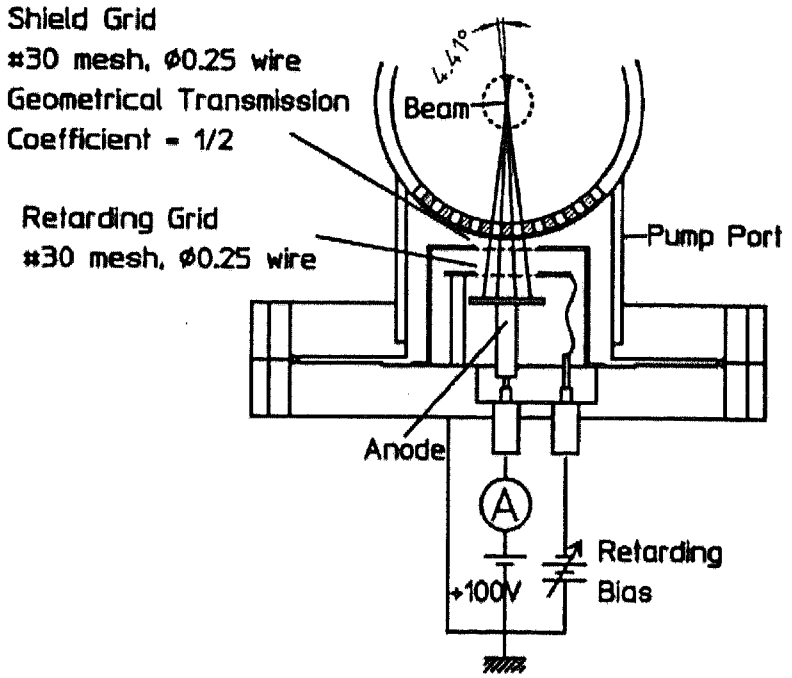

Fig. 3.1. Schematic drawing of a KEKB LER pump port and the RFA [67].

3.1.2 Structure of the electron monitor

Fig. 3.2b shows a worm's eye view of the pump port in a field-free region of the LER chamber. It has a rectangular metallic frame that consists of straight metallic strips. These strips are covered by a set of 2-mm-thick angular metallic pipes placed at right angles to them. The cage-like structure is thus divided into a mesh of rectangular holes. The retarding grid and the anode assembly are mounted on a stainless-steel flange.

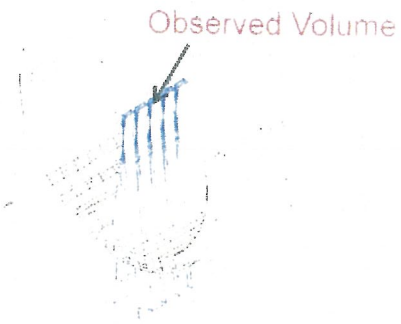

Fig. 3.2a. Schematic drawing of near-beam observed volume [67].

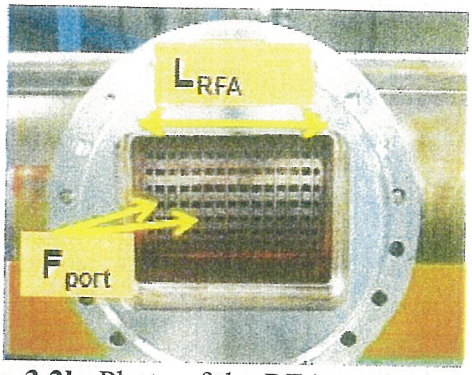

Fig. 3.2b. Photo of the RFA entrance in a field-free region of the LER chamber [67].

The length of the RFA entrance assembly along the LER chamber is $L_{RFA} = 0.1\ m$. The presence of the rectangular slot holes make the energetic electrons leave the RFA entrance from a restricted length defined by L_{obs}. There are ten horizontal slots, each having fifteen holes. Each hole, 5 *mm* in length, is separated by a 2 *mm* thick angular metallic pipe. Therefore, by geometry,

$$L_{obs} = 0.072\ m. \qquad (3.1)$$

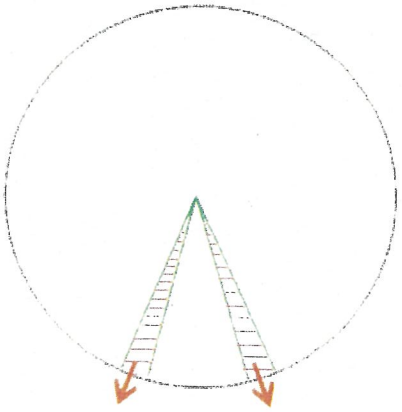

Fig. 3.3. The hatched region defines F_{port} in the schematic cross-section of the LER chamber containing RFA entrance. The angular width of each hole (shown by arrows on the chamber wall) is 4 *mm*.

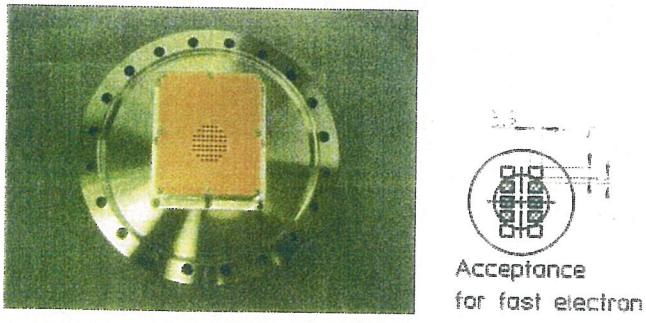

Fig. 3.4. Photograph of the electron monitor (left) and dimensions of its holes (right) [67].

The electron monitor is mounted on a vacuum pump port of the LER chamber vertically down the beam axis, and the electrons enter it through an array of rectangular holes, i.e., the RFA entrance, arranged along longitudinal slots on the chamber wall. Each hole is 5 *mm* in length and 4 *mm* in angular width. The electrons leaving the two central slot holes only (Figs. 3.2a and 3.3) are detected at the monitor. This restriction introduces a cross-sectional area reduction factor represented by F_{port}. The radius of the LER chamber is 47 *mm* and each slot hole has an angular opening of 4 *mm*. Therefore,

$$F_{port} = 2 \times \frac{4\ mm}{2 \times \pi \times 47\ mm} \cong 0.0271. \qquad (3.2)$$

Not all the electrons passing through the two central slot holes of the RFA entrance contribute to monitor yield. Fig. 3.4 shows a photograph of an electron monitor. It contains a fine mesh of holes. The electrons striking the monitor, that pass through these fine holes, contribute to the yield. These fine holes on the monitor, therefore, reduce the monitor current by a factor defined as monitor aperture reduction factor, represented by F_{mon}. By geometry of the fine holes on the monitor, $F_{mon} = 0.26$.

3.1.3 Analytic formalism of the measurement method

In past the data taken by RFA with a multi-channel plate showed that the signal had peaks coinciding with the bunch pattern if a high voltage of –2 *kV* is applied to the retarding grid [67]. This suggests that a peak corresponding to high-energy component of the EC is accredited to those electrons located near the beam and kicked towards the center of the LER chamber by a passing bunch. If the beam is assumed to have a uniform longitudinal line charge density with no transverse

dimensions, then the kick experienced by an electron at a radial distance r from a passing bunch is given by

$$\Delta p = \frac{2r_e}{r} N_b m_e c, \tag{3.3}$$

where r_e is the classical electron radius and Δp is the change in the momentum of the electron after experiencing a beam kick. Since most electrons have a low energy [89], if r is sufficiently small, the kick [eq. (3.3)] is the final momentum of the electron. The electrons near the beam experience a strong beam kick that overcomes the space charge repulsive force. We, therefore, neglected the effect hereafter.

The retarding bias voltage limits the detected electrons to those that gained a kinetic energy more than or equal to eV_b after receiving a beam kick. V_b and r are related by

$$eV_b = \frac{\Delta p^2}{2m_e} = 2\frac{r_e^2}{r^2} N_b^2 m_e c^2. \tag{3.4}$$

Assuming that the detected electrons were stationary at the time of experiencing a beam kick and that they entered the monitor in a single kick, the volume occupied by them immediately before receiving the kick, defined as an observed volume of the detected electrons at the electron monitor, is given by [using eq. (3.4)]

$$V_{obs}(V_b) = A\pi r^2 = 2\pi A r_e^2 N_b^2 \frac{m_e c^2}{eV_b}, \tag{3.5}$$

where A is the acceptance of the electrons at the monitor, and V_{obs}, the observed volume. Average ECD, represented by ρ_{ave}, is given by

$$\rho_{ave} = Y_m(V_b)/V_{obs}(V_b), \tag{3.6}$$

where Y_m is the number of energetic electrons per bunch detected at the electron monitor.

3.2 Simulation of the measurement

We discussed in sec. 3.1.2 that the energetic electrons detected by the monitor are limited by its acceptance. As mentioned in sec. 2.5, we numerically tracked the macro-electrons, which are much smaller in number than the actual electrons. The acceptance of the real monitor is quite small and at low bunch currents, only a small number of macro-electrons would be counted at the electron monitor, which might lead to a numerical noise. We, therefore, did not model the actual electron monitor. Instead, we considered the two central slot holes of the RFA entrance as monitor and numerically counted the number of macro-electrons entering into it. Therefore, $F_{mon} = 1$. The value of A, i.e., the acceptance of macro-electrons at the two central slot holes of the RFA entrance, based on the effective length and the angular width of the slot holes, is given by [using eqs. (3.1) and (3.2)]

$$A = L_{obs} \cdot F_{port} \cdot F_{mon} = 0.072m \times 0.0271 \times 1 \cong 1.95 \times 10^{-3} m. \qquad (3.7)$$

In section 3.1.3, we discussed that the analytic estimate of an observed volume of the detected electrons is based on certain assumptions. Since the energetic electrons emanate from a near-beam region, therefore to validate the assumptions, the backtracking of the detected electrons at the two central slot holes of the RFA entrance is essential. It can be achieved by numerical simulations only.

3.2.1 Numerical backtracking of the energetic electrons

We added a subroutine in our code to numerically backtrack the energetic macro-electrons from the wall inside the LER chamber till their last interaction with the beam. In Fig. 3.5, a transverse distribution, resulting from backtracking of the macro-electrons from the entire periphery of the chamber wall till they received last beam kick, is shown for V_b = -1 kV, i_B = 1.2 mA, a bunch train of 200, and δ_{max} = 1.2.

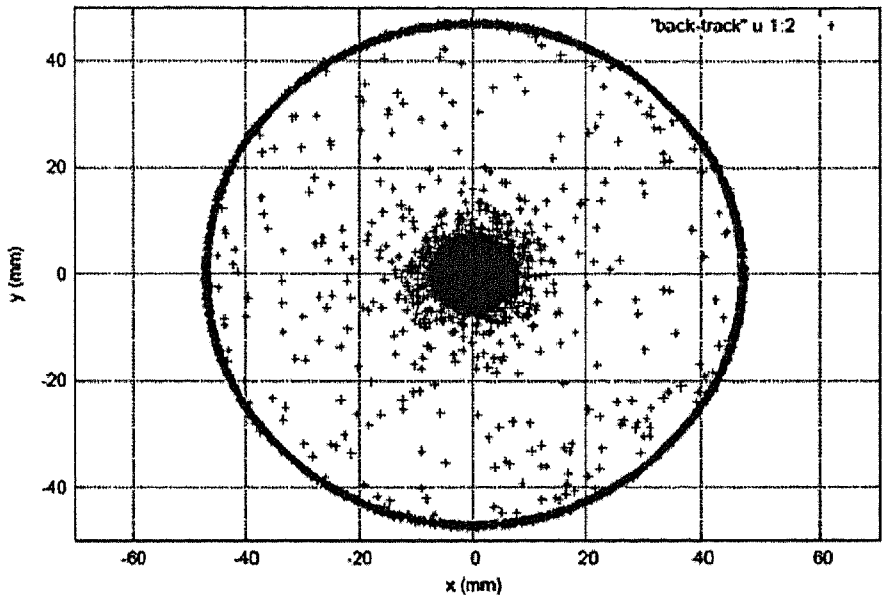

Fig. 3.5. *x-y* distribution of backtracked macro-electrons from entire chamber wall inside the LER chamber till their last beam interaction. V_b = -1 kV, i_B = 1.2 mA.

Bulks of them seem to occupy a circular region around the beam within a radius of less than 7 mm.

The bunch population N_b is related to bunch current i_B by

$$i_B = eN_b f_{rev}. \qquad (3.8)$$

Using eqs. (3.4) and (3.8), an expression for r, the radius of a cylinder concentric with the LER chamber, containing the electrons with energy $\geq eV_b$ is given by

$$r = r_e \frac{i_B}{e f_{rev}} \sqrt{\frac{2m_e c^2}{eV_b}}. \qquad (3.9)$$

For $V_b = 1\ kV$, $i_B = 1.2\ mA$ and $f_{rev} = 99.4\ kHz$, the value of $r \sim 6.8$ mm, which agreed quite well with the simulation result (Fig. 3.5). In reality, the macro-electrons hitting a fraction of the periphery of the chamber wall contribute yield to the electron monitor. We shall discuss the backtracking of macro-electrons from the RFA entrance till their last interaction with the beam, in the next section. Such electrons are henceforth referred as the 'backtracked' electrons.

3.2.2 Observed volume in simulations

As stated earlier, the beam kick is assumed to be the final momentum of an electron [eq. (3.3)]. This means that electrons can be treated as stationary at the time of experiencing a beam kick. In the stationary electron approximation, the observed volume of the backtracked electrons is expected to be a straight cone. To examine this, we considered a hypothetical RFA entrance located exactly at the bottom of the LER chamber. The model assumed an opening of ±2 *mm* around the vertical axis and a bias voltage of -1 *kV* as shown in Fig. 3.6.

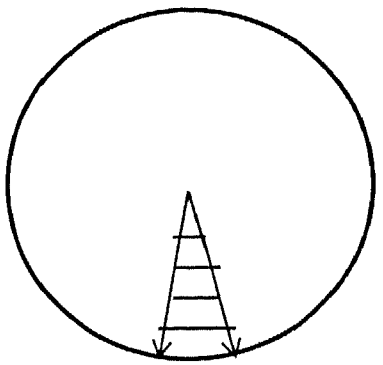

Fig. 3.6. Cross-section of the LER chamber with a hypothetical 4 *mm* angular opening (shown as hatched area).

All the electrons, that hit the hypothetical opening, were numerically backtracked inside the LER chamber till they received the last beam kick. Fig. 3.7 shows an example of the *x-y* distribution of the backtracked electrons detected at the hypothetical opening. The background dots represent a uniform distribution of all the stationary electrons in an arbitrarily chosen area. The shaded region represents a distribution of the detected electrons immediately before receiving the beam kick. It has a shape of a straight cone as expected.

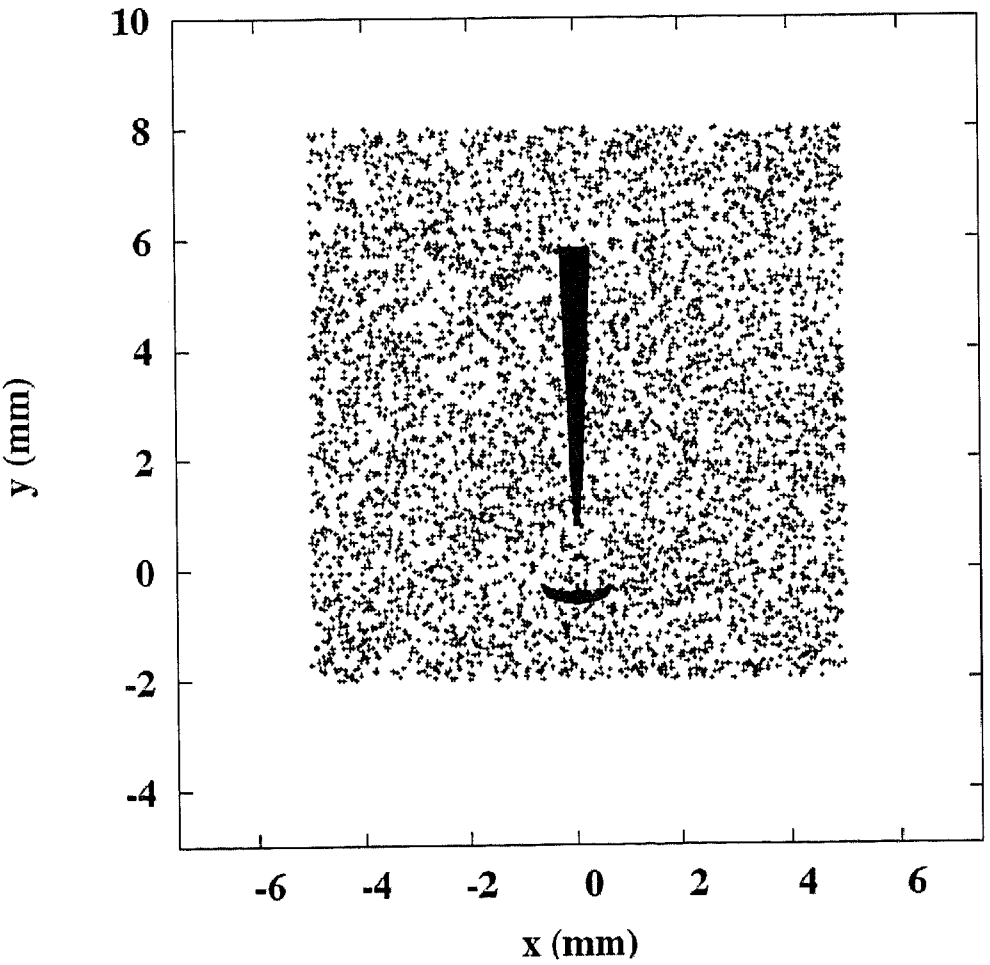

Fig. 3.7. *x-y* distribution of the backtracked electrons (shaded in black) under stationary electron approximation.

In reality, however, the electrons have nonzero velocities. Considering the finite velocities of the electrons at the time of the beam kick, the *x*-*y* distribution of the observed volume of the detected electrons has a highly deformed cone like structure, as shown in Fig. 3.8. The model assumed the same hypothetical opening (Fig. 3.6) and the bias voltage.

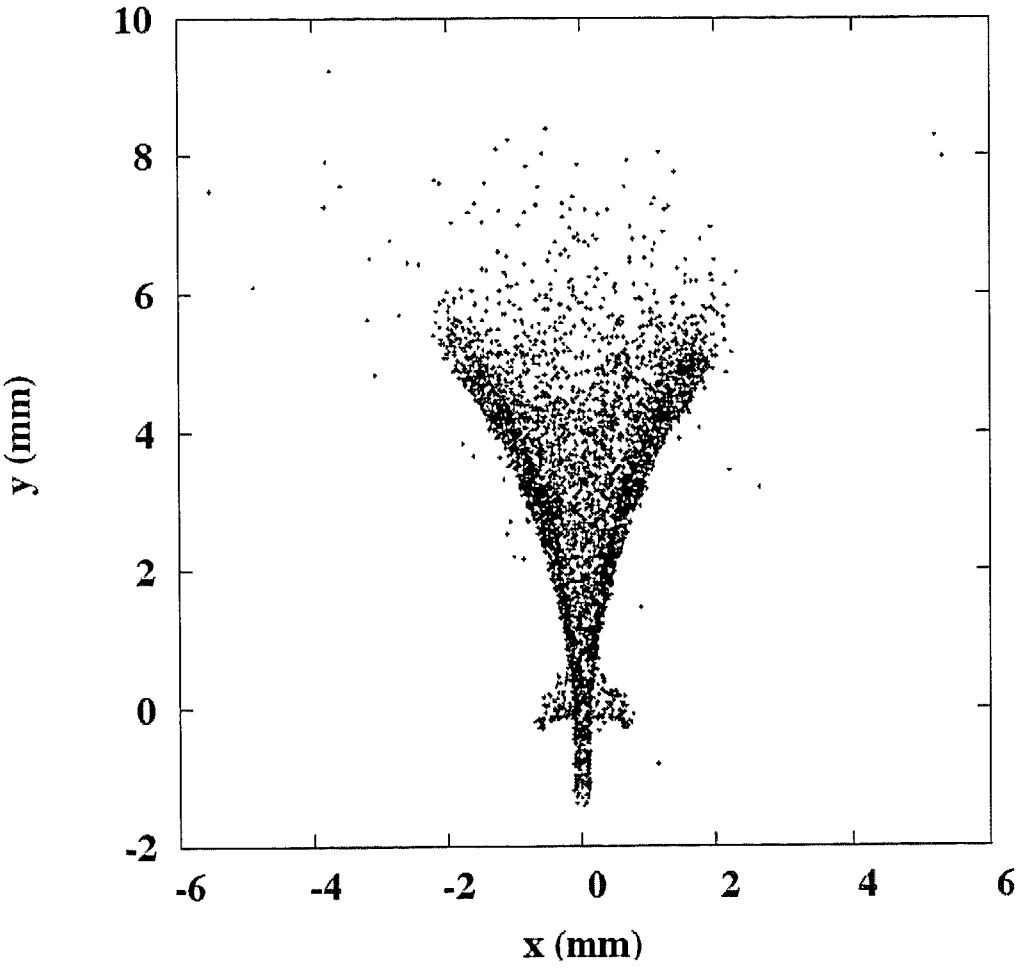

Fig. 3.8. *x*-*y* distribution of the backtracked electrons considering their finite velocities at beam kick.

It also reveals that the *x*-*y* distribution has two branches. This deformation in the shape was examined analytically.

We derive a general equation of the trajectory of an electron, which has a finite velocity before getting a beam kick, and, that enters into an arbitrary RFA opening, say (x_m, y_m), on the LER chamber. Consider an electron at a location (x, y) with a velocity (v_x, v_y) at the time of receiving the beam kick v_k as shown in Fig. 3.9.

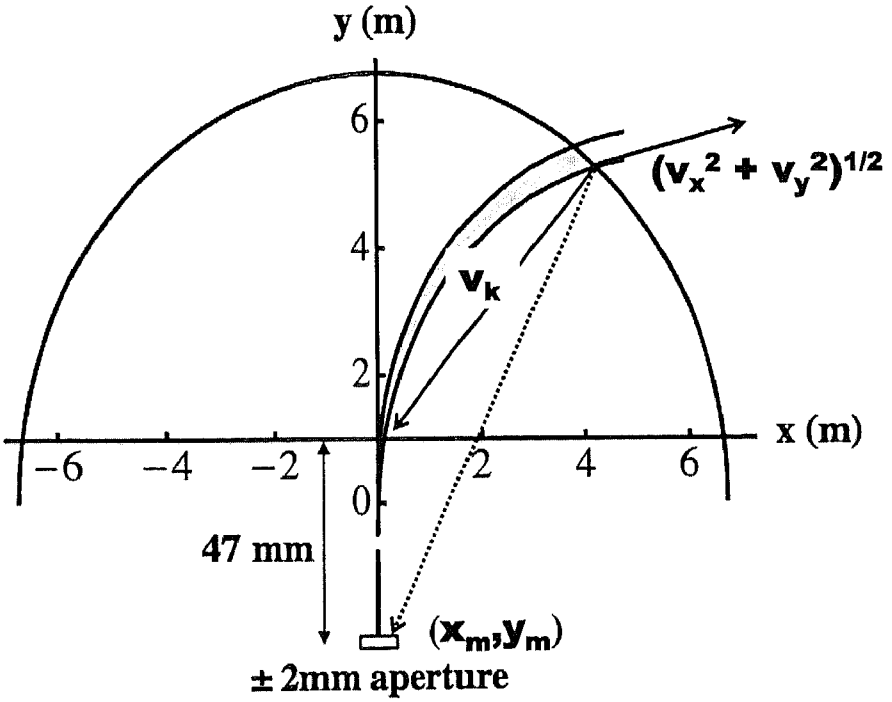

Fig. 3.9. Calculation of an area where detected electrons are located. v_k is the velocity received from the beam kick. Curves bounding the shaded region are plotted using eq. (3.11).

Let the kicked electron be detected at (x_m, y_m). By relating the direction of the resultant of two velocities (shown in dotted line in Fig. 3.9) with that defined by (x, y) and (x_m, y_m) gives an expression

$$(x^2 + y^2)[(y - y_m)v_x - (x - x_m)v_y] + 2cr_eN_b(xy_m - yx_m) = 0, \qquad (3.10)$$

which is a general equation of the locus of a moving electron, which enters an arbitrary opening (x_m, y_m) on the LER chamber wall after the beam kick. In Fig. 3.9, the loci of kicked electrons entering the hypothetical opening between (-2, - 47 *mm*) and (2, - 47 *mm*), are shown by two curves, which are obtained using eq. (3.10). A shaded region bounded by these two curves represents an area corresponding to an observed volume of the detected electrons.

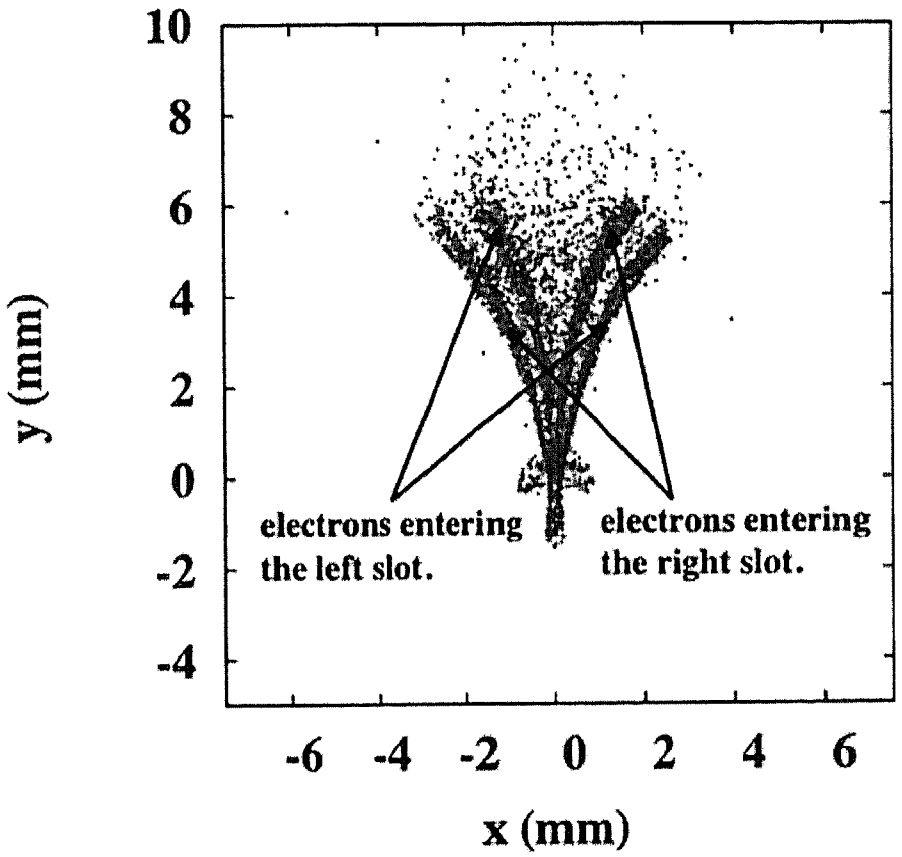

Fig. 3.10. *x-y* distribution of the backtracked electrons detected at the RFA entrance with two central slot holes. The bias voltage is -1 *kV*.

If v_x is taken to be negative, a mirror-symmetrical curve about *y*-axis is obtained. For the RFA entrance with two central slot holes (Figs. 3.2a and 3.3) on the LER chamber, the *x-y* distribution of an observed volume of the detected electrons, with a

bias voltage of -1 kV, is shown in Fig. 3.10. For two slot holes, there are four branches in the x-y distribution. The calculations further showed that v_y does not markedly deform the shaded region in Fig. 3.9.

3.2.3 Calculation of near-beam ECD by simulations

We added a module into our code to calculate the ECD as seen by the beam. We chose a $\delta_{max} = 1.2$. We ran the code for 200 bunch passes under different bunch currents ranging from 0.2 mA to 1.2 mA. Experimentally one measures a time-averaged near beam ECD density as seen by the beam. To get it from the simulations, the EC was first allowed to build-up for 199 bunch passes. The density estimation was done during the 200th bunch pass. As mentioned in sec. 3.2.1 the radius of the cylinder r, concentric with the LER chamber, containing the electrons with energy $\geq eV_b$, is given by eq. (3.9). The volume of this cylinder of an arbitrary length L (for example, L of 19.78 mm was chosen in our model) is $V_d = \pi r^2 L$. We numerically counted the number of macro-electrons confined in a cylinder of radius r and length L during the 200th bunch pass at different bunch locations (for example, 348 locations, uniformly distributed inside the CBX, were chosen in our model) for V_b = -1 kV. Let their average be represented by N_m. The average density of the near-bunch EC is obtained using

$$\rho_{ave} = \frac{N_m}{V_d}. \qquad (3.11)$$

Figs. 3.11a and 3.11b show the z-x and z-y distribution of the backtracked electrons respectively at a time of the 200th bunch entering into the CBX. It is seen that the near-beam electrons are mainly populated in the beginning of the CBX, and, as the

bunch propagates the zone of the near-beam electrons also propagates along the beam (Fig. 3.11a). This means

$$\frac{1}{L}\int \rho(0,0,z,t_0)\,dz \neq \frac{1}{L}\int \rho\left(0,0,z',\frac{z'}{c}\right)dz', \tag{3.12}$$

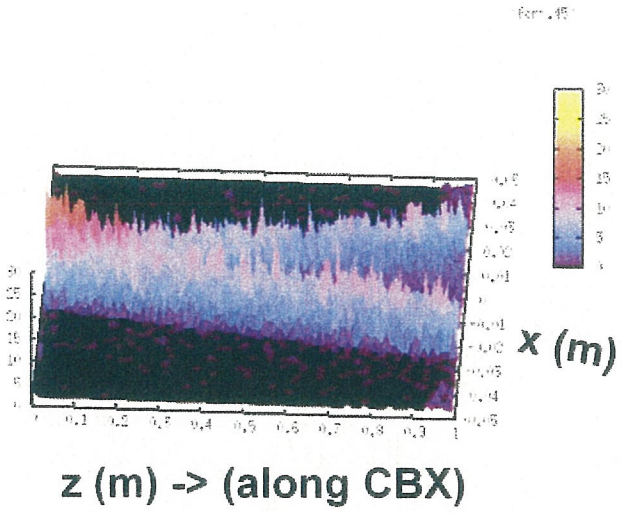

Fig. 3.11a. *z-x* distribution of the backtracked electrons when the 200th bunch just entered inside the CBX. V_b = -1 *kV*, i_B = 1.2 *mA* and δ_{max} = 1.2.

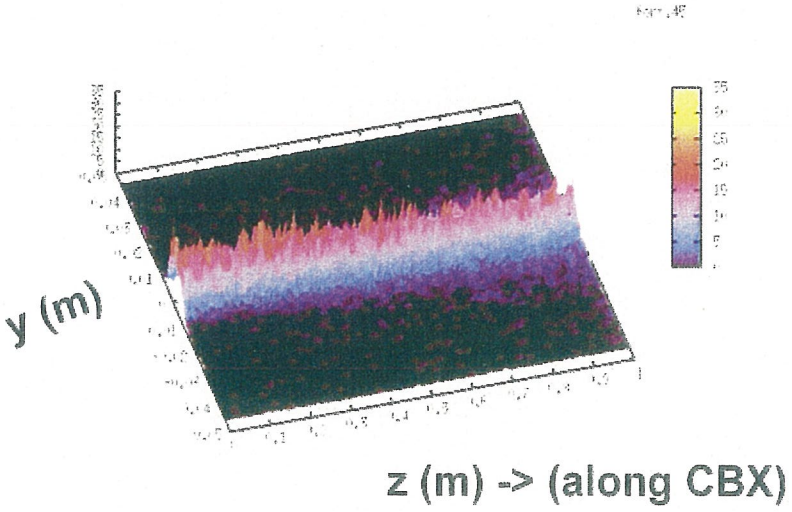

Fig. 3.11b. *z-y* distribution of the backtracked electrons when the 200th bunch just entered inside the CBX. V_b = -1 *kV*, i_B = 1.2 *mA* and δ_{max} = 1.2.

The z-y distribution of the backtracked electrons, however, does not support this fact. The near-beam electrons are seen to be uniformly distributed along the CBX (Fig. 3.11b). The difference in z-x and z-y distributions, as shown in Figs. 3.11a and 3.11b, is due to the fact that v_y does not affect the observed volume as compared to v_x. Further, the method ensures to calculate the near-beam ECD as seen by the beam.

3.2.4 Comparison of the observed volumes

We now examine how the deformed observed volume of the macro-electrons detected at the two central slot holes of the RFA entrance (Figs. 3.2a and 3.3) obtained by the simulations deviates from that obtained using the analytic formula [eq. (3.5)]. Instead of comparing the volumes, we compare V_{obs}/i_B^2 since it is a constant and easy to compare as a function of the bunch current i_B.

From eqs. (3.5) and (3.8), one can deduce an observed volume per unit square of bunch current represented by V_{obs}/i_B^2, which is independent of bunch parameters and is expressed as

$$\frac{V_{obs}(V_b)}{i_B^2} = 100.795 \times 10^3 \frac{A}{V_b}, \qquad (3.13)$$

where $V_b(Volt)$, $A(meter)$, $i_B(Ampere)$, $V_{obs}(meter^3)$ are the bias potential, acceptance of electrons at the two central slot holes of the RFA entrance, bunch current and the observed volume, respectively. The analytic value of V_{obs}/i_B^2 is [using eqs. (3.13) and (3.7)]

$$V_{obs}(V_b)/i_B^2 \cong 0.197\ meter^3/Amp^2, \qquad (3.14)$$

for V_b of -1 kV.

As discussed in sec. 3.1.3, if Y_m represents the number of macro-electrons per bunch counted numerically at the two central slot holes of the RFA entrance, then the simulated value of V_{obs}/i_B^2 can be expressed as [using eq. (3.6)]

$$\frac{V_{obs}(V_b)}{i_B^2} = \frac{Y_m/\rho_{ave}}{i_B^2}, \tag{3.15}$$

where ρ_{ave} is calculated using eq. (3.11).

We calculated the simulated value of V_{obs}/i_B^2 [using eq. (3.15)] for different bunch currents. Fig. 3.12 shows a comparison of the V_{obs}/i_B^2 values obtained by simulations [eq. (3.15)] and using the analytic formula [eq. (3.14)], as a function of bunch current.

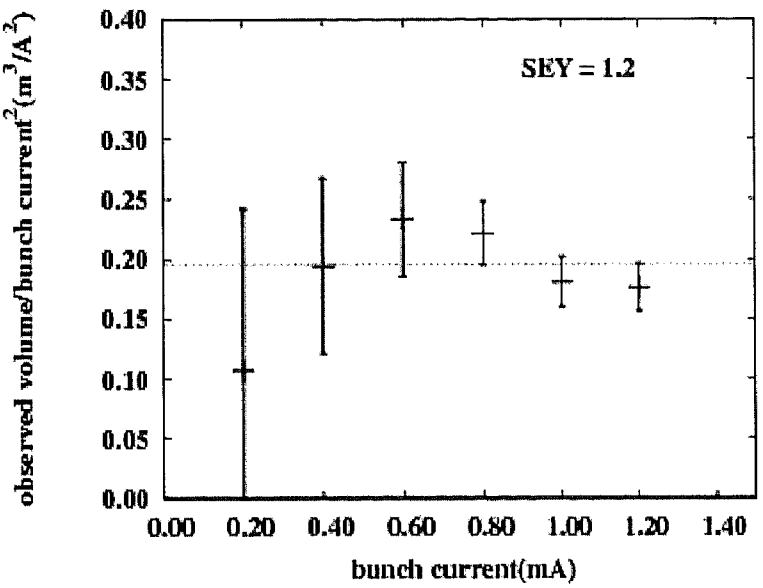

Fig. 3.12. Observed volume per unit square of the bunch current obtained by the simulation (shown with vertical bars). A dotted line shows the analytic value [eq. (3.14)]. $\delta_{max} = 1.2$, $V_b = -1\ kV$, and bunch separation = 6 ns.

Error bars are the statistical errors calculated from the number of the detected macro-electrons. The dotted line is the value obtained from eq. (3.14). V_{obs}/i_B^2, obtained by simulations is almost the same as that obtained by analytic estimation assuming that

the electrons are stationary, despite the fact that the nonzero velocities of the electrons deformed the shape of the observed volume. This leads to a conclusion that the simple method of the measurement of the ECD near the beam can still be applied.

The simulations were repeated for $\delta_{max} = 0.96$ and $\delta_{max} = 1.4$.

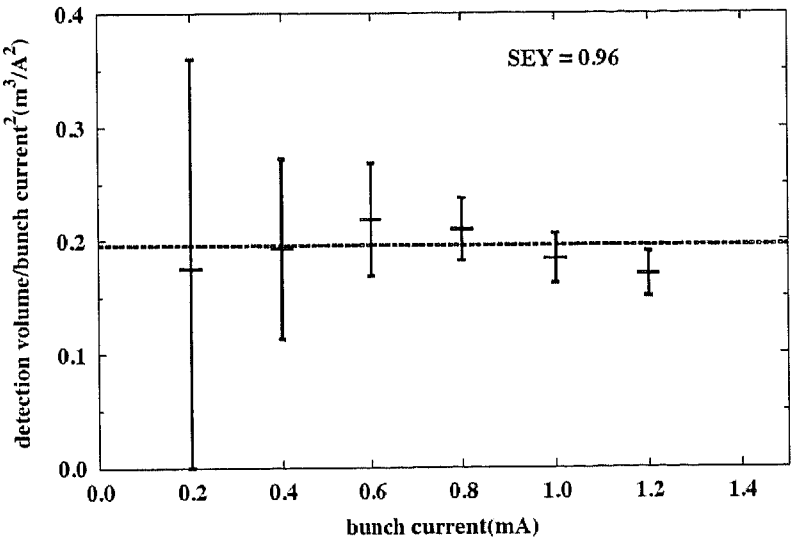

Fig. 3.13. Observed volume per unit square of the bunch current obtained by the simulation (shown with vertical bars). A dotted line shows the analytic value [eq. (3.14)]. $\delta_{max} = 0.96$, $V_b = -1\ kV$, and bunch separation = 6 ns.

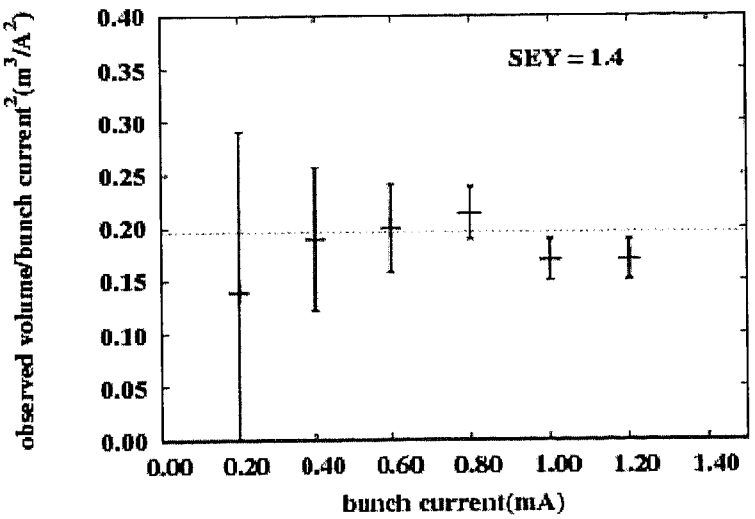

Fig. 3.14. Observed volume per unit square of the bunch current obtained by the simulation (shown with vertical bars). A dotted line shows the analytic value [eq. (3.14)]. $\delta_{max} = 1.4$, $V_b = -1\ kV$, and bunch separation = 6 ns.

Figs. 3.13 and 3.14 show a similar comparison for δ_{max} = 0.96 and δ_{max} = 1.4 respectively. From the plots we conclude that V_{obs} / i_B^2 obtained by simulations is significantly consistent with the analytic formalism and that it is independent of SEY.

3.2.5 Validity of the analytic formalism

In sec. 3.2.4, it was shown that V_{obs} / i_B^2 estimated by the numerical simulations agreed quite well with the analytic formalism (Figs. 3.12, 3.13 and 3.14). The value of V_{obs} / i_B^2 obtained by simulation relied on the validity of the expression given by eq. (3.6). In this section we shall discuss the reason why the analytic estimate is valid even the velocity distribution of electrons deforms the shape of the observed volume (sec. 3.2.2).

Next, we examine the conditions under which the method in sec. 3.1 can be applied more generally. For simplicity of the analysis, we discuss only the 2-dimensional motion of electrons. We consider the length of the RFA entrance having any arbitrary slot openings to be unity. Therefore, the formula, corresponding to eq. (3.6), which is to be examined, is

$$S_{obs} = Y_m / \rho_{ave}, \qquad (3.16)$$

where S_{obs} is the observed area of the backtracked electrons from the RFA entrance in the x-y plane calculated assuming initially stationary electrons. Let $\rho(x, y, v_x, v_y, t_0)$ represents the phase space density of the electrons, where t_0 refers to the time immediately before the last electron-beam interaction before the electrons are detected. The two-dimensional average density of the EC near the beam can be expressed as

$$\rho_{ave} = \frac{\int_{\vec{v}} \int_{S_D} \rho(x, y, v_x, v_y, t_0) dx\, dy\, dv_x\, dv_y}{S_D}, \qquad (3.17)$$

where S_D is the area covered by the near-beam electrons with an energy larger than or equal to eV_b at the time of the beam kick. The integration limit $\vec{v}(v_x, v_y)$ in eq. (3.17) corresponds to all possible velocities of the electrons confined in the area S_D. The schematic of S_D is shown in Fig. 3.15a. The backtracked electrons from the RFA entrance occupy a velocity dependent area, represented by $S(\vec{v})$, which is shown in Fig. 3.15b.

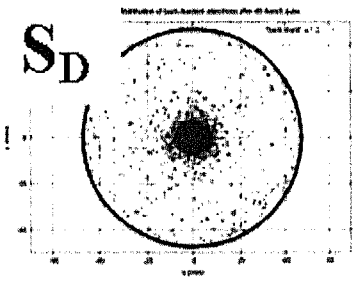

Fig. 3.15a. Schematic of S_D.

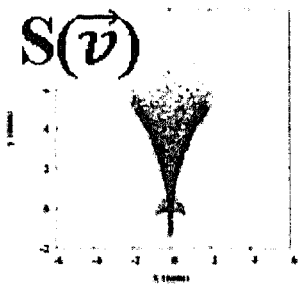

Fig. 3.15b. Schematic of $S(\vec{v})$.

The beam kick experienced by the electrons is a conservative force, therefore, according to Liouville's theorem; the density of electrons is same in Figs. 3.15a and 3.15b, which is given by eq. (3.17). The number of electrons per bunch that entered the RFA, Y_m, is expressed as

$$Y_m = \int_{S(\vec{v})} dx'\, dy'\, \rho_{ave}$$

$$= \int_{S_D} dx'\, dy' \frac{\int_{\vec{v}} \int_{S(\vec{v})} \rho(x, y, v_x, v_y, t_0) dx\, dy\, dv_x\, dv_y}{S_D}$$

$$= \int_{\vec{v}} dv_x\, dv_y \int_{S(\vec{v})} \rho(x, y, v_x, v_y, t_0) dx\, dy, \qquad (3.18)$$

where $S(\vec{v})$, included in S_D, is an area roughly corresponding to a region near the bunch containing the electrons with energy $\geq eV_b$. Let us define the function $D(\vec{v})$ as

$$D(\vec{v}) \equiv \frac{1}{\rho_{ave}\, S_D} \int_{S_D} \rho(x, y, v_x, v_y, t_0) dx\, dy, \tag{3.19}$$

where $D(\vec{v})$ satisfies the condition

$$\int_{\vec{v}} D(\vec{v})\, dv_x\, dv_y = 1. \tag{3.20}$$

Using $D(\vec{v})$, we define the function $\Delta(x, y, v_x, v_y)$ as

$$\rho(x, y, v_x, v_y, t_0) \equiv \rho_{ave}\, D(\vec{v}) + \Delta(x, y, v_x, v_y), \tag{3.21}$$

which satisfies the condition

$$\int_{\vec{v}} dv_x\, dv_y \int_{S_D} \Delta(x, y, v_x, v_y) dx\, dy = 0. \tag{3.22}$$

Then, Y_m can be rewritten as

$$\begin{aligned} & Y_m \\ & = \int_{\vec{v}} dv_x\, dv_y \int_{S(\vec{v})} dx\, dy \left[\rho_{ave}\, D(\vec{v}) + \Delta(x, y, v_x, v_y)\right] \\ & = \rho_{ave} \int_{\vec{v}} S(\vec{v})\, D(\vec{v})\, dv_x\, dv_y \\ & + \int_{\vec{v}} dv_x\, dv_y \int_{S(\vec{v})} dx\, dy\, \Delta(x, y, v_x, v_y). \end{aligned} \tag{3.23}$$

Equation (3.23) shows that, if the conditions

$$\int_{\vec{v}} S(\vec{v})\, D(\vec{v})\, dv_x\, dv_y = S_0 \cong S_{obs}, \tag{3.24}$$

and

$$R = \frac{\int_{\vec{v}} dv_x\, dv_y \int_{S(\vec{v})} \Delta(x, y, v_x, v_y)\, dx\, dy}{\rho_{ave}\, S_0} \ll 1, \tag{3.25}$$

are satisfied, we obtain $Y_m \sim \rho_{ave}\, S_{obs}$. S_0, a velocity-independent term in eq. (3.24), is the observed area of the backtracked electrons from the RFA entrance under stationary electron approximation, i.e., S_{obs}. A schematic of S_{obs} is shown in Fig. 3.15c.

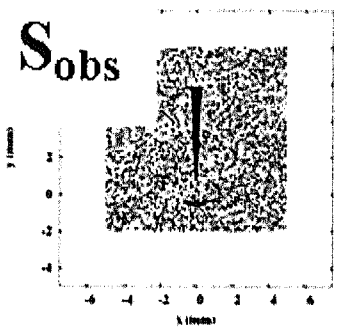

Fig. 3.15c. Schematic of S_{obs}.

To examine the conditions of eq. (3.24) in our case, the shaded area in Fig. 3.9 was numerically integrated for v_x and v_y, varying between 0 to 1.4×10^7 m/s and -1×10^6 to 1×10^6 m/s, respectively, and compared with the arc in Fig. 3.8. An approximate calculation, as shown in Fig. 3.16, tells that the difference in the areas is within ±5%. Thus,

$$\int_{\vec{v}} S(\vec{v})\, D\,(\vec{v})\, dv_x\, dv_y \cong S_{obs} \int_{\vec{v}} D(\vec{v})\, dv_x\, dv_y = S_{obs}. \tag{3.26}$$

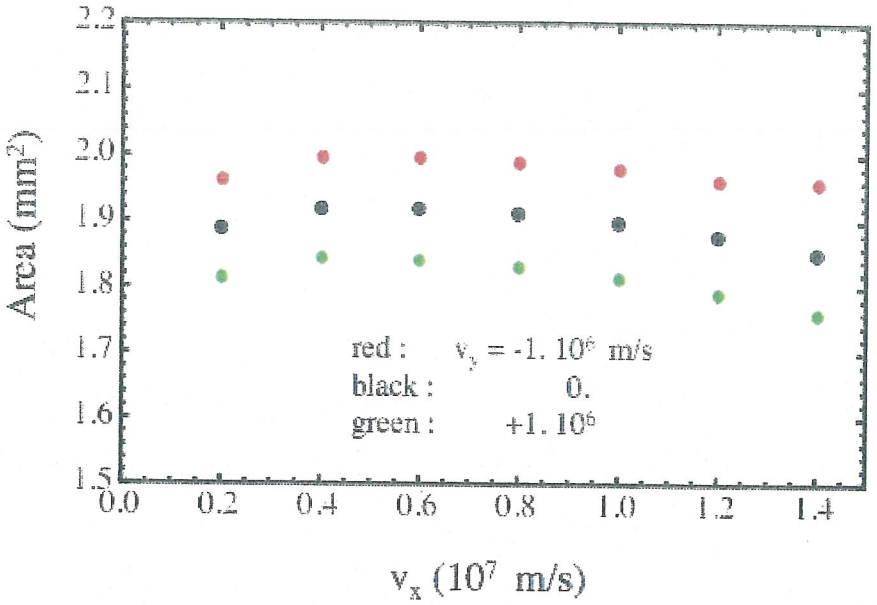

Fig. 3.16. Effect of non-stationary electron consideration on observed volume.

To examine the conditions of eq. (3.25), R was calculated using the ECD distribution at a bunch current of 1.2 mA, and using $S(v_x, v_y)$ for $v_x = 1\times10^7$ m/s and $v_y = 0$ m/s, respectively. Then, we obtained $R = 0.01$. The conditions of eq. (3.25) are also reasonably valid in our case.

In this formalism the assumption by Kanazawa *et al.* is expressed as

$$D(v_x, v_y) = \delta(v_x)\,\delta(v_y), \tag{3.27}$$

where δ is the Dirac delta function and R ~ 0. Therefore, we obtain

$$\int_{\vec{v}} S(\vec{v})\,D\,(\vec{v})\,dv_x\,dv_y = S(0), \tag{3.28}$$

which shows that the left-hand side of eq. (3.24) is exactly the same as the observed volume of stationary electrons.

3.2.6 Effect of the background electrons

It is possible that some electrons might be detected from outside the near-bunch region. The number of such electrons, defined as the background electrons, introduces a measurement error. To estimate this error, the energetic electrons detected at the two central slot holes of the RFA entrance were backtracked at a bunch current of 1.2 *mA* and $\delta_{max} = 1.2$.

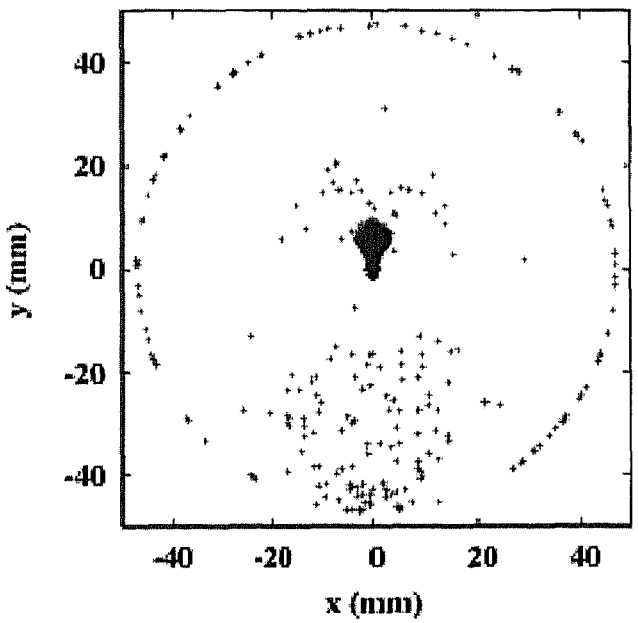

Fig. 3.17. *x-y* distribution of the backtracked electrons for i_B=1.2 mA, $\delta_{max} = 1.2$.

Fig. 3.17 shows the electrons outside the near-beam region. The number of such electrons, expressed as $N(r)$, is estimated by integrating the number of backtracked

electrons as a function of r, where r is the radial distance measured from the central region outside the near-beam up to the chamber radius. Analytically, $N(r)$ is expressed as

$$N(r) = \int_{r}^{r_{chm}} dr' N_{bk-tr}(r'). \tag{3.29}$$

Fig. 3.18 shows a plot of the number of backtracked electrons versus r. The number of background electrons is estimated to be ~ 5% of the total backtracked electrons.

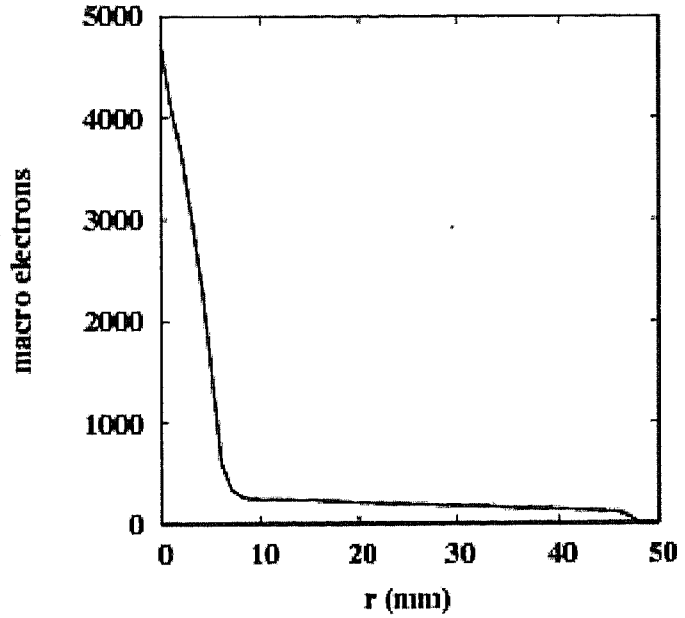

Fig. 3.18. Number of backtracked electrons versus r.

3.2.7 Comparison of the near-beam ECD of measurements and analytic formalism with the simulations

Fig. 3.19a shows a comparison of the near-beam ECD obtained by the simulations with that obtained by the analytic formalism coupled with the experimental data as a function of bunch-current. A bunch-spacing of 6 *ns*, a train of 200 bunches and δ_{max} = 1.2 were chosen for the comparison. We mentioned in sec. 2.1.4 that the sources of macro-photoelectrons from the reflected synchrotron light were uniformly distributed on the entire circumference of the LER chamber with a reflectivity of 20%. We, however, kept the reflectivity of the surface and the sources of macro-photoelectrons as free parameters.

The red curve shows the measured density. The near-beam ECD curve increases monotonously. The experimental data is available for bunch currents ranging from 0.2 *mA* to 1.1 *mA*. The blue curve shows a simulated ECD for a 20% reflectivity of the photons from the LER surface that generated macro-photoelectrons uniformly distributed on the entire circumference of the LER chamber. The simulated density agrees well with the measurement till a bunch current of 0.7 *mA*. Beyond that the simulated density saturates and decreased with an increase in the bunch current. The simulation conditions were changed for the sources of the macro-photoelectrons from the reflected light. The green curve shows a simulated ECD for a 20% reflectivity of the photons that generate macro-photoelectrons uniformly distributed in a vertical angular opening of 60 degree centered at the beam-axis. There was no change observed in the simulated ECD from the previous case. Next, we changed the simulation conditions with no sources of macro-photoelectrons from the reflected light. The pink curve shows a simulated ECD for zero reflectivity of the photons. The densities were slightly smaller than the ones in the previous two cases; however, the trend of the ECD pattern did not change.

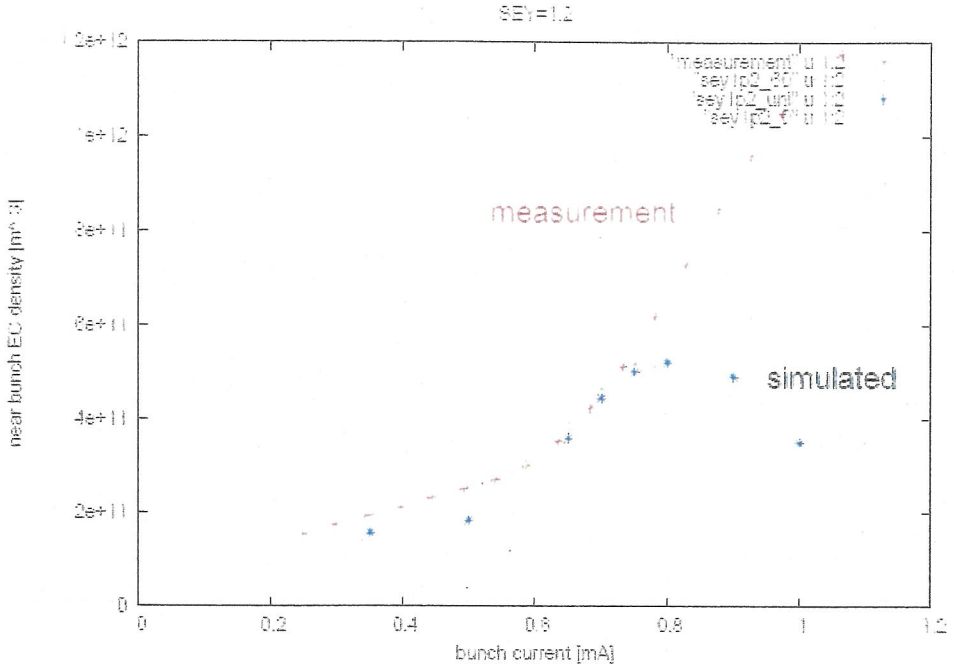

Fig. 3.19a. Comparison of ECD between analytic calculation and simulations. δ_{max} = 1.2, bunch spacing = 6 *ns*, no. of bunches = 200.

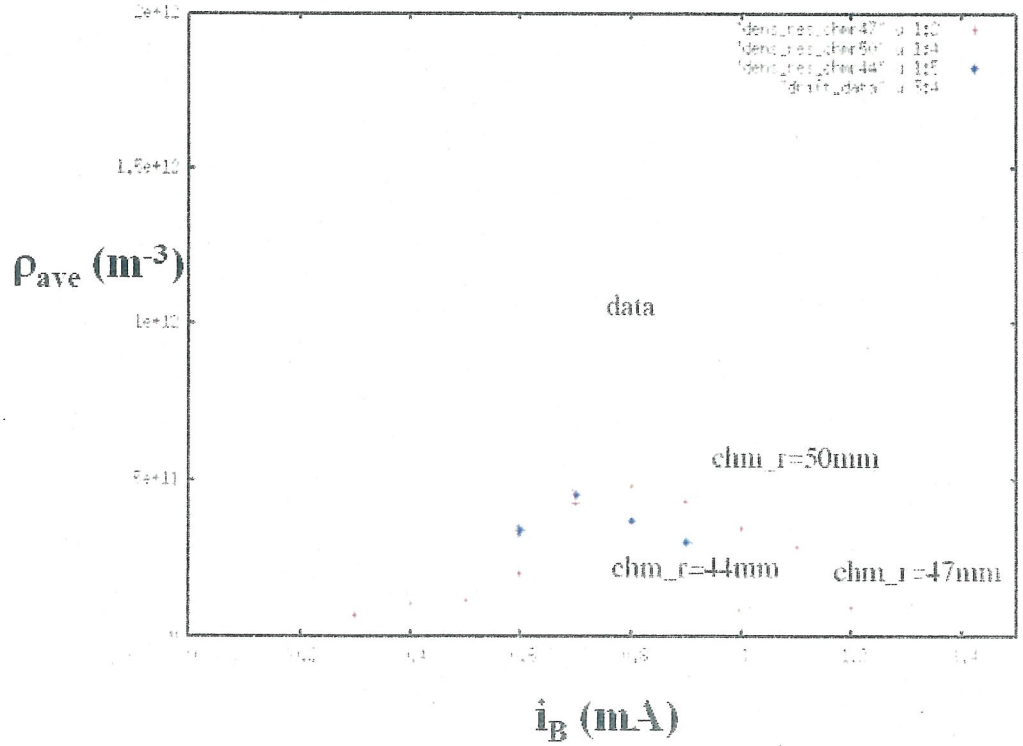

Fig. 3.19b. Comparison of ECD between analytic calculation and simulations. Radius of LER chamber = 0.047 *m*, 0.044 *m* and 0.05 *m*. Other simulation conditions were kept same.

All the three simulated densities show a saturation at $i_B = 0.8\ mA$, beyond which they tend to decrease. The simulations confirmed that there is hardly any effect of the reflectivity of the surface on the near-beam ECD calculations.

To understand the reason for saturation of density at $i_B = 0.8\ mA$ and beyond, the simulations were carried out for two different choices of radius of the LER chamber, viz, 0.044 m and 0.05 m, respectively. The other beam conditions were kept same as earlier. The results are shown in Fig. 3.19b. The blue curve, corresponding to chamber radius of 0.044 m, shows saturation in density at $i_B = 0.8\ mA$ whereas, the green curve, corresponding to chamber radius of 0.05 m, shows saturation in density at $i_B = 1.0\ mA$.

In simulations, we assumed that the beam is always on the center of the LER chamber; however, in reality there can be an offset in the beam position, which could change the results on near-beam ECD as seen in Fig. 3.19b.

Chapter 4: CONCLUSION

We analyzed the method of the measurement of the near-beam ECD developed by Kanazawa *et al.* The conclusion of the work is summarized below:

- A detailed analysis for the validity of near-beam ECD has been carried out with a newly developed simulation code by the author at KEK laboratory.

- Backtracking of the detected electrons and ECD as seen by the beam are the main features of our code.

- It was found that the shape of V_{obs} near the beam was highly deformed by the horizontal velocity distribution of electrons; nevertheless the analytic formalism was still applicable to obtain the EC density. This agreement was well understood by detailed analysis.

- According to this analysis and the data taken in KEKB LER, EC density is determined to be $1\times10^{12}\ m^{-3}$ in drift region without solenoid field at bunch current of 1 mA within an accuracy of 10%. A density of $5\times10^{11}\ m^{-3}$ is (roughly) a threshold value for single bunch instability to occur for KEKB beam parameters. This work will contribute to develop the mitigation techniques against the EC.

The ECD measured near the beam with the analytic formalism was compared with that calculated by the simulation. The result showed that

1) The simulated ECD agreed well with the measured values for bunch currents lesser than 0.8 mA for a $\delta_{max} = 1.2$.
2) The fact mentioned in 1) was also observed at different δ_{max} values, with no significant change in the density values.

3) The positions of the macro-photoelectrons from the reflected synchrotron light did not affect the ECD.
4) The choice of reflectivity of the surface also did not affect the result.
5) The disagreement of 1) was not caused by the method of the measurement but by some other physical reasons, possibly due to non consideration of the offset of the beam, because we showed that the analytic formula to calculate the observed volume can be applied at least up to a bunch current of 1.2 *mA*.

A detailed comparison between the measurement and the simulation is a subject of future study. The measurement of the near-beam electron cloud density in a quadrupole magnet is going on in KEKB LER. The analysis of the measurement method in a quadrupole will be interesting and important to interpret the data.

References

1) J. Rees: Colliders, in Handbook of Accelerator Physics and Engineering, World Scientific (1998) pp. 11-13.

2) D. W. Kerst, F. T. Cole, H. R. Crane, L. W. Jones, et al.: Phys. Rev. **102**, No. 2 (1956) 590.

3) Tihiro Ohkawa: Part. Accel., U.S. Patent 2890348, June 9, 1959.

4) Gerard K. O'Neill: Phys. Rev. **102** (1956) pp. 1418-1419.

5) Gerald P. Jackson: Nucl. Instrum. Methods Phys. Res., Sect. A **408** (1998) 296.

6) S. Guiducci: Nucl. Instrum. Methods Phys. Res., Sect. A **461** (2001) 1.

7) Junji Haba: Nucl. Instrum. Methods Phys. Res., Sect. A **368** (1995) 74.

8) Toru Iijima: Nucl. Instrum. Methods Phys. Res., Sect. A **446** (2000) 65.

9) S. Kurokawa, and E. Kitutani: Nucl. Instrum. Methods Phys. Res., Sect. A **499** (2003) 1.

10) K. Akai et al.: Nucl. Instrum. Methods Phys. Res., Sect. A **499** (2003) 191.

11) KEK 2010 report: [http://www-acc.kek.jp/kekb/].

12) H. Fukuma et al.: Proc. EPAC'2000 Conf., Vienna (2000) 1122.

13) H. Fukuma et al.: Proc. High Energy Accelerator Conf. (HEACC 2001), Tsukuba (2001).

14) F. Zimmermann: Rep. No. CERN-SL-Note-2000-004 AP (2000).

15) K. Ohmi and F. Zimmermann: Phys. Rev. Lett. **85** (2000) 3821.

16) K. Ohmi, F. Zimmermann, and E. Perevedentsev: Phys. Rev. E **65** (2001) 016502.

17) Proc. of the ECLOUD'02, ECLOUD'04 and ECLOUD'07 workshops.

18) F. Zimmermann: CERN Rep. No. CERN-LHC-PROJECT-REPORT-95, SLAC Rep. No. SLAC-PUB-7425, 1997.

19) O. Gröbner: Rep. No. CERN-LHC-PROJECT-REPORT-127 (1997).

20) G. Budker, G. Dimov, and V. Dudnikov: Sov. Atom. E. **22** (1967) 5.

21) J. H. Martin, R. A. Winje, R. H. Hilden, and F. E. Mills: Proc. Fifth Int. Conf. High-Energy Accelerators (HEACC 65), Frascati (1965) 347.

22) E. C. Raka: Proc. Sixth Int. Conf. High-Energy Accelerators (HEACC 67), Cambridge (1967) 428.

23) H. A. Grunder and G. R. Lambertson: presented at the Eighth Int. Conf. High-Energy Accelerators (HEACC 71), Geneva (1971).

24) R. Calder, E. Fischer, O. Gröbner, and E. Jones: Proc. Ninth Int. Conf. High-Energy Accelerators (HEACC 74), Stanford (1974) pp. 70-74.

25) D. Neuffer et al.: Nucl. Instrum. Methods Phys. Res., Sect. A **321** (1992) 1.

26) R. L. Macek, A. Brownman, D. Fitzgerald, R. McCrady, F. Merril, M. Plum, T. Spickermann, T. S. Wang, J. Griffin, K. Y. Ng, D. Wildman, K. Harkay, R. Kustom, and R. Rosenberg: Proc. Particle Accelerator Conf. (PAC'01), Chicago (2001) 688.

27) M. Izawa et al.: Phys. Rev. Lett. **74** (1995) 5044.

28) K. Ohmi: Phys. Rev. Lett. **75** (1995) 1526.

29) L. E. Sakazaki, R. M. Littauer, R. H. Siemann, and R. M. Talman: IEEE Trans. Nucl. Sci. **32** (1985) 2353.

30) M. G. Billing, M. Giannella, R. M. Littauer, and G. R. Rouse: Proc. IEEE Particle Accelerator Conf. (PAC'89), Chicago (1989) 1163.

31) Hartill, T. Holmquist, J. T. Rogers, and D. C. Sagan: Cornell LNS Rep. CBN 95-3 (1995).

32) J. T. Rogers: Proc. Particle Accelerator Conf. (PAC'95), Dallas (1995) 3052.

33) T. Holmquist and J. T. Rogers: Proc. EPAC'1996 Conf., Barcelona (1996) 319.

34) T. Holmquist and J. T. Rogers: Phys. Rev. Lett. **79** (1997) 3186.

35) Z. Y. Guo at al.: Proc. Particle Accelerator Conf. IEEE (PAC'97), Vancouver (1997) 1566.

36) Q. Qin et al.: Nucl. Instrum. Methods Phys. Res., Sect. A **547** (2005) 239.

37) K. Akai et al.: Proc. Particle Accelerator Conf. IEEE (PAC'99), New York (1999) 288.

38) M. A. Furman and G. R. Lambertson: Proc. Particle Accelerator Conf. IEEE (PAC'97), Vancouver (1997) 1617.

39) O. Bruning: Proc. EPAC'1998 Conf., Stockholm (1996) 332.

40) O. Gröbner: Vacuum **47** (1996) 591.

41) O. Bruning, F. Caspers, I. R. Collins, O. Gröbner, B. Henrist, N. Hilleret, J. M. Laurent, M. Morvillo, M. Pivi, F. Ruggiero, and X. Jhang: Proc. Particle Accelerator Conf. (PAC'99), New York (1999) pp. 2629-2631.

42) G. Arduini et al.: Proc. EPAC'2000 Conf., Vienna (2000) pp. 259-261.

43) V. Baglin, J. Bojko, O. Gröbner, B. Henrist, N. Hilleret, C. Scheuerlein, and M. Taborelli: Proc. EPAC'2000 Conf., Vienna (2000) pp. 217-219.

44) G. Stupakov and M. Pivi: ECLOUD'04 Workshop, Napa (2004).

45) K. Oide: CERN Rep. No. SL-2001-003 (2001).

46) Y. Suetsugu et al.: J. Vac. Sci. Technol. **21** (2003) 186.

47) Y. Suetsugu et al.: Nucl. Instrum. Methods Phys. Res., Sect. A **538** (2005) 206.

48) V. Baglin, I. R. Collins, and O. Gröbner: Proc. EPAC'1998 Conf., Stockholm (1998) pp. 2169-2171.

49) G. Arduini, J. M. Jimenez, and K. Weiss: Proc. Particle Accelerator Conf. (PAC'01), Chicago (2001) 685.

50) F. Le Pimpec et al.: Nucl. Instrum. Methods Phys. Res., Sect. A **564** (2006) 44.

51) Y. Suetsugu et al.: Nucl. Instrum. Methods Phys. Res., Sect. A **578** (2007) 470.

52) K. Ohmi and S. Matsumoto: Proc. First Asian Particle Accelerator Conf. (APAC'98), Tsukuba (1998) pp. 435-437.

53) G. Rumolo, F. Zimmermann, H. Fukuma, and K. Ohmi: Proc. Particle Accelerator Conf. (PAC'01), Chicago (2001) pp. 1889-1891.

54) Y. Suetsugu, Y. Tanimoto, Y. Hori, K. Kanazawa, and M. Kobayashi: Proc. Particle Accelerator Conf. (PAC'01), Chicago (2001) pp. 2180-2182.

55) L. F. Wang et al.: Phys. Rev. ST Accel. Beams **7** (2004) 034401.

56) F. Pedersen, A. Poncet, and L. Soby: Proc. Particle Accelerator Conf. (PAC'89), Chicago **3** (1989) 1786.

57) M. Venturini, M. Furman, J-L. Vay, and M. Pivi: Proc. Particle Accelerator Conf. (PAC'07), Albuquerque (2007) pp. 2993-2995.

58) M. Pivi, F. K. King, R. E. Kirby, T. Markiewicz, T. O. Raubenheimer, J. Seeman, and L. Wang: Proc. EPAC'08 Conf., Genoa (2008) pp. 691-693.

59) Y. Suetsugu, H. Fukuma, K. Shibata, M. Pivi, and L. Wang: Proc. First Int. Particle Accelerator Conf. (IPAC'10), Kyoto (2010) pp. 2021-2023.

60) Y. Suetsugu, H. Fukuma, K. Shibata, M. Pivi, and L. Wang: Proc. First Int. Particle Accelerator Conf. (IPAC'10), Kyoto (2010) pp. 4689-4691.

61) P. Thieberger et al.: Phys. Rev. ST Accel. Beams 7 (2004) 093201.

62) S. Y. Zhang et al.: Phys. Rev. ST Accel. Beams **8** (2005) 123201.

63) R. J. Macek, R. McCrady, S. B. Walbridge, T. Zaugg, C. Deibele, S. Henderson, M. A. Plum, S. Assadi, J. Byrd, S. Y. Lee, and M. F. T. Pivi: The 39th ICFA Adv. Beam Dynamics Workshop High Intensity High Brightness Hadron Beams (HB2006), Tsukuba (2006) pp. 94-98.

64) R. J. Macek et al.: Phys. Rev. ST Accel. Beams **11** (2008) 010101.

65) M. K. Covo et al.: Phys. Rev. Lett. **97** (2006) 054801.

66) S. De Santis et al.: Phys. Rev. Lett. **100** (2008) 094801.

67) K. Kanazawa, H. Fukuma, H. Hisamatsu, and Y. Suetsugu: Proc. Particle Accelerator Conf. (PAC'05), Knoxville (2005) 1054.

68) M. Sands: SLAC Rep. No. SLAC-0121 (1970).

69) Robert H. Day: AIP Conf. Proc. **75** (1981) 44.

70) A. Hofmann: CERN Accelerator School Proc., CERN 98-04 (1998).

71) H. Seiler: J. App. Phys. Vol. **54**, R1 (1983).

72) M. A. Furman and G. R. Lambertson: Proc. Int. Workshop Multibunch Instabilities in Future Electron and Positron Accelerators (MBI97), Tsukuba (1997) 170.

73) G. Rumolo et al.: Phys. Rev. ST Accel. Beams **4**, (2001) 012801.

74) G. Dugan and D. Sagan: SYNRAD3D Manual [http://www.lepp.cornell.edu/~dcs/synrad3d.pdf].

75) B. L. Henke, E. M. Gullikson, and G. C. Davis: At. Data Nucl. Data Tables **54** (1993) 181.

76) M. Bassetti and G. Erskine: CERN-ISR-TH/80-06 (1980).

77) J. D. Jackson: *Classical Electrodynamics*, Chap. 11; John Wiley & Sons Inc.

78) K. S. Kölbig: *Complex error function*, Program C 335CERN, Geneva (1970).

79) K. Ohmi [private communication].

80) R. E. Kirby and F. K. King: Nucl. Instrum. Methods Phys. Res., Sect. A **469** (2001) 1.

81) M. A. Furman and M. T. F. Pivi: Phys. Rev. ST Accel. Beams **5** (2002) 124404.

82) A. J. Dekker: *Secondary Electron Emission*, edited by F. Seitz and D. Turnbull, Solid State Physics Vol. 6, Academic Press, New York (1958), pp. 251-315.

83) P. A. Redhead, J. P. Hobson, and E. V. Kornelsen: *The Physical Basis of Ultrahigh Vacuum*, Chapman and Hall, London (1968).

84) H. Bruining: *Physics and Applications of Secondary Electron Emission*, Pergamon Press, McGraw-Hill Book Co., New York (1954).

85) V. Baglin, I. Collins, B. Henrist, N. Hilleret, and G. Vorlaufer: CERN LHC Proj. Rep. No. 472 [unpublished].

86) Erwin Kreyszig: *Advanced Engineering Mathematics*, Chapter 21; Numerics for ODEs and PDEs; Wiley Publishers.

87) R. W. Hockney and J. W. Eastwood: *Computer Simulation Using Particles*, Chapter 6; Taylor and Francis Publishers (1989).

88) W. H. Press, S. A. Teukolsky, W. T. Vetterling, and B. P. Flannery: *Numerical Recipes in C*, Secs. 16.1 and 16.2, Cambridge University Press, New Delhi (2008).

89) H. Fukuma: Proc. Mini-Workshop Electron-Cloud Simulations for Proton and Positron Beams (ECLOUD02), Geneva (2002) 1.